

1

²A SEARCH FOR LONG-LIVED, CHARGED, SUPERSYMMETRIC PARTICLES
³USING IONIZATION WITH THE ATLAS DETECTOR

4

BRADLEY AXEN

5

September 2016 – Version 0.27

6



⁸ Bradley Axen: *A Search for Long-Lived, Charged, Supersymmetric Particles using Ion-
⁹ ization with the ATLAS Detector*, Subtitle, © September 2016

10

Usually a quotation.

11

Dedicated to.

₁₂ ABSTRACT

₁₃ How to write a good abstract:

₁₄ <https://plg.uwaterloo.ca/~migod/research/beck00PSLA.html>

₁₅ PUBLICATIONS

₁₆ Some ideas and figures have appeared previously in the following publications:

₁₇

₁₈ Put your publications from the thesis here. The packages `multibib` or `bibtopic`
₁₉ etc. can be used to handle multiple different bibliographies in your document.

²¹ ACKNOWLEDGEMENTS

²² Put your acknowledgements here.

²³

²⁴ And potentially a second round.

²⁵

26 CONTENTS

27	I	INTRODUCTION	1
28	1	INTRODUCTION	3
29	II	THEORETICAL CONTEXT	5
30	2	STANDARD MODEL	7
31	2.1	Particles	7
32	2.2	Interactions	8
33	2.3	Limitations	8
34	3	SUPERSYMMETRY	9
35	3.1	Motivation	9
36	3.2	Structure	9
37	3.3	Phenomenology	9
38	4	LONG-LIVED PARTICLES	11
39	4.1	Mechanisms	11
40	4.1.1	Examples in Supersymmetry	11
41	4.2	Phenomenology	11
42	4.2.1	Disimilarities to Prompt Decays	11
43	4.2.2	Characteristic Signatures	11
44	III	EXPERIMENTAL STRUCTURE AND RECONSTRUCTION	13
45	5	THE LARGE HADRON COLLIDER	15
46	5.1	Injection Chain	15
47	5.2	Design and Parameters	15
48	5.3	Luminosity	15
49	6	THE ATLAS DETECTOR	17
50	6.1	Coordinate System	17
51	6.2	Magnetic Field	17
52	6.3	Inner Detector	17
53	6.3.1	Pixel Detector	17
54	6.3.2	Semiconductor Tracker	17
55	6.3.3	Transition Radiation Tracker	17
56	6.4	Calorimetry	17
57	6.4.1	Electromagnetic Calorimeters	17
58	6.4.2	Hadronic Calorimeters	17
59	6.4.3	Forward Calorimeters	17
60	6.5	Muon Spectrometer	17
61	6.6	Trigger	17
62	6.6.1	Trigger Scheme	17
63	6.6.2	Missing Transverse Energy Triggers	17
64	7	EVENT RECONSTRUCTION	19
65	7.1	Tracks and Vertices	19

66	7.1.1	Track Reconstruction	19
67	7.1.2	Vertex Reconstruction	19
68	7.2	Jets	19
69	7.2.1	Topological Clustering	19
70	7.2.2	Jet Energy Scale	19
71	7.2.3	Jet Energy Scale Uncertainties	19
72	7.2.4	Jet Energy Resolution	19
73	7.3	Electrons	19
74	7.3.1	Electron Identification	19
75	7.4	Muons	19
76	7.4.1	Muon Identification	19
77	7.5	Missing Transverse Energy	19
78	IV	CALORIMETER RESPONSE	21
79	8	RESPONSE MEASUREMENT WITH SINGLE HADRONS	23
80	8.1	Dataset and Simulation	24
81	8.1.1	Data Samples	24
82	8.1.2	Simulated Samples	24
83	8.1.3	Event Selection	24
84	8.2	Inclusive Hadron Response	25
85	8.2.1	E/p Distribution	26
86	8.2.2	Zero Fraction	26
87	8.2.3	Neutral Background Subtraction	28
88	8.2.4	Corrected Response	28
89	8.3	Identified Particle Response	34
90	8.3.1	Decay Reconstruction	34
91	8.3.2	Identified Response	35
92	8.3.3	Additional Species in Simulation	37
93	8.4	Summary	38
94	9	JET ENERGY RESPONSE AND UNCERTAINTY	41
95	9.1	Motivation	41
96	9.2	Uncertainty Estimate	41
97	9.3	Summary	44
98	V	SEARCH FOR LONG-LIVED PARTICLES	47
99	10	LONG-LIVED PARTICLES IN ATLAS	49
100	10.1	Overview and Characteristics	49
101	10.2	Simulation	49
102	11	EVENT SELECTION	51
103	11.1	Trigger	52
104	11.2	Kinematics and Isolation	52
105	11.3	Standard Model Rejection	56
106	11.4	Ionization	58
107	11.4.1	Mass Estimation	59
108	11.5	Summary	60
109	12	BACKGROUND ESTIMATION	63

110	12.1	Background Sources	63
111	12.2	Prediction Method	63
112	12.3	Validation and Uncertainty	63
113	13	SYSTEMATIC UNCERTAINTIES AND RESULTS	65
114	13.1	Systematic Uncertainties	65
115	13.2	Final Yields	65
116	14	INTERPRETATION	67
117	14.1	Cross Sectional Limits	67
118	14.2	Mass Limits	67
119	14.3	Context for Long-Lived Searches	67
120	VI	CONCLUSIONS	69
121	15	SUMMARY AND OUTLOOK	71
122	15.1	Summary	71
123	15.2	Outlook	71
124	VII	APPENDIX	73
125	A	INELASTIC CROSS SECTION	75
126	B	APPENDIX TEST	77
127	B.1	Appendix Section Test	77
128	B.1.1	Appendix Subection Test	77
129	B.2	A Table and Listing	77
130	B.3	Some Formulas	78
131		BIBLIOGRAPHY	81

132 LIST OF FIGURES

133	Figure 1	The particle content of the Standard Model (SM).	8
134	Figure 2	An illustration (a) of the E/p variable used throughout this paper. The red energy deposits come from the charged particle targeted for measurement, while the blue energy deposits are from nearby neutral particles and must be subtracted. The same diagram (b) for the neutral-background selection, described in Section 8.2.3.	25
135			
136			
137			
138			
139			
140	Figure 3	The E/p distribution and ratio of simulation to data for isolated tracks with (a) $ \eta < 0.6$ and $1.2 < p/\text{GeV} < 1.8$ and (b) $ \eta < 0.6$ and $2.2 < p/\text{GeV} < 2.8$	26
141			
142			
143	Figure 4	The fraction of tracks as a function (a, b) of momentum, (c, d) of interaction lengths with $E \leq 0$ for tracks with positive (on the left) and negative (on the right) charge.	27
144			
145			
146			
147	Figure 5	$\langle E/p \rangle_{\text{BG}}$ as a function of the track momentum for tracks with (a) $ \eta < 0.6$, (b) $0.6 < \eta < 1.1$, and as a function of the track pseudorapidity for tracks with (c) $1.2 < p/\text{GeV} < 1.8$, (d) $1.8 < p/\text{GeV} < 2.2$	29
148			
149			
150			
151	Figure 6	$\langle E/p \rangle_{\text{COR}}$ as a function of track momentum, for tracks with (a) $ \eta < 0.6$, (b) $0.6 < \eta < 1.1$, (c) $1.8 < \eta < 1.9$, and (d) $1.9 < \eta < 2.3$	30
152			
153			
154	Figure 7	$\langle E/p \rangle_{\text{COR}}$ calculated using LCW-calibrated topological clusters as a function of track momentum for tracks with (a) zero or more associated topological clusters or (b) one or more associated topological clusters.	31
155			
156			
157			
158	Figure 8	Comparison of the $\langle E/p \rangle_{\text{COR}}$ for tracks with (a) less than and (b) greater than 20 hits in the TRT.	32
159			
160	Figure 9	Comparison of the $\langle E/p \rangle_{\text{COR}}$ for (a) positive and (b) negative tracks as a function of track momentum for tracks with $ \eta < 0.6$	32
161			
162			
163	Figure 10	Comparison of the E/p distributions for (a) positive and (b) negative tracks with $0.8 < p/\text{GeV} < 1.2$ and $ \eta < 0.6$, in simulation with the FTFP_BERT and QGSP_BERT physics lists.	33
164			
165			
166			
167	Figure 11	Comparison of the response of the hadronic calorimeter as a function of track momentum (a) at the EM-scale and (b) after the LCW calibration.	33
168			
169			
170	Figure 12	Comparison of the response of the EM calorimeter as a function of track momentum (a) at the EM-scale and (b) with the LCW calibration.	34
171			
172			

173	Figure 13	The reconstructed mass peaks of (a) K_S^0 , (b) Λ , and (c) $\bar{\Lambda}$ candidates.	35
174			
175	Figure 14	The E/p distribution for isolated (a) π^+ , (b) π^- , (c) proton, and (d) anti-proton tracks.	36
176			
177	Figure 15	The fraction of tracks with $E \leq 0$ for identified (a) π^+ and π^- , and (b) proton and anti-proton tracks	36
178			
179	Figure 16	The difference in $\langle E/p \rangle$ between (a) π^+ and π^- (b) p and π^+ , and (c) \bar{p} and π^-	37
180			
181	Figure 17	$\langle E/p \rangle_{\text{COR}}$ as a function of track momentum for (a) π^+ tracks and (b) π^- tracks.	38
182			
183	Figure 18	The ratio of the calorimeter response to single parti- cles of various species to the calorimeter response to π^+ with the physics list FTFP_BERT.	38
184			
185	Figure 19	The spectra of true particles inside anti- k_t , $R = 0.4$ jets with (a) $90 < p_T/\text{GeV} < 100$, (b) $400 < p_T/\text{GeV} <$ 500 , and (c) $1800 < p_T/\text{GeV} < 2300$	42
186			
187	Figure 20	The jet energy scale (JES) uncertainty contributions, as well as the total JES uncertainty, as a function of jet p_T for (a) $ \eta < 0.6$ and (b) $0.6 < \eta < 1.1$	44
188			
189	Figure 21	The JES correlations as a function of jet p_T and $ \eta $ for jets in the central region of the detector.	45
190			
191	Figure 22	The distribution of E_T^{miss} for data and simulated signal events, after the trigger requirement.	53
192			
193	Figure 23	The dependence of dE/dx on N_{split} in data after basic track hit requirements have been applied.	54
194			
195	Figure 24	The distribution of dE/dx with various selections ap- plied in data and simulated signal events.	55
196			
197	Figure 25	The distribution of track momentum for data and sim- ulated signal events, after previous selection require- ments have been applied.	55
198			
199	Figure 26	The distribution of M_T for data and simulated sig- nal events, after previous selection requirements have been applied.	56
200			
201	Figure 27	The distribution of summed tracked momentum within a cone of $\Delta R < 0.25$ around the candidate track for data and simulated signal events, after previous selec- tion requirements have been applied.	57
202			
203	Figure 28	The normalized, two-dimensional distribution of E/p and f_{EM} for simulated (a) $Z \rightarrow ee$, (b) $Z \rightarrow \tau\tau$, (c) 1200 GeV Stable R-Hadron events, and (d) 1200 GeV, 10 ns R-Hadron events.	58
204			
205	Figure 29	Two-dimensional distribution of dE/dx versus charge signed momentum (qp) for minimum-bias tracks. The fitted distributions of the most probable values for pi- ons, kaons and protons are superimposed.	59
206			

218	Figure 30	The distribution of mass estimated using dE/dx for simulated stable R-Hadrons with masses between 1000 and 1600 GeV.	60
219			
220			

221 LIST OF TABLES

222	Table 1	The dominant sources of corrections and systematic 223 uncertainties in the JES estimation technique, includ- 224 ing typical values for the correcting shift (Δ) and the 225 associated uncertainty (σ).	43
226	Table 2	The expected number of events at each level of the se- 227 lection for metastable 1600 GeV, 10 ns R-Hadrons, 228 along with the number of events observed in data, for 229 3.2 fb^{-1} . The simulated yields are shown with statis- 230 tical uncertainties only. The total efficiency \times accep- 231 tance is also shown for the signal.	61
232	Table 3	Autem usu id	77

²³³ LISTINGS

²³⁴ Listing 1	A floating example (<code>listings</code> manual)	78
--------------------------	--	----

235 ACRONYMS

236 SM Standard Model

237 LSP Lightest Supersymmetric Particle

238 LHC Large Hadron Collider

239 ToT time over threshold

240 LCW local cluster weighted

241 MIP minimally ionizing particle

242 EPJC European Physical Journal C

243 JES jet energy scale

244 LLP Long-Lived Particle

245

PART I

246

INTRODUCTION

247

You can put some informational part preamble text here.

1

248

249 INTRODUCTION

250

PART II

251

THEORETICAL CONTEXT

252

You can put some informational part preamble text here.

2

253

254 STANDARD MODEL

255 The SM of particle physics seeks to explain the symmetries and interactions of
256 all currently discovered fundamental particles. It has been tested by several genera-
257 tions of experiments and has been remarkably successful, no significant de-
258 viations have been found. The SM provides predictions in particle physics for
259 interactions up to the Planck scale (10^{15} - 10^{19} GeV).

260 The theory itself is a quantum field theory grown from an underlying $SU(3) \times$
261 $SU(2) \times U(1)$ that requires the particle content and quantum numbers consist-
262 ent with experimental observations (see Section 2.1). Each postulated symme-
263 try is accompanied by an interaction between particles through gauge invari-
264 ance. These interactions are referred to as the Strong, Weak, and Electromag-
265 netic forces, which are discussed in Section 2.2.

266 Although this model has been very predictive, the theory is incomplete; for
267 example, it is not able to describe gravity or astronomically observed dark matter.
268 These limitations are discussed in more detail in Section 2.3.

269 21 PARTICLES

270 The most familiar matter in the universe is made up of protons, neutrons, and
271 electrons. Protons and neutrons are composite particles, however, and are made
272 up in turn by particles called quarks. Quarks carry both electric charge and color
273 charge, and are bound in color-neutral combinations called baryons. The elec-
274 tron is an example of a lepton, and carries only electric charge. Another type
275 of particle, the neutrino, does not form atomic structures in the same way that
276 quarks and leptons do because it carries no color or electric charge. Collectively,
277 these types of particles are known as fermions, the group of particles with half-
278 integer spin.

279 There are three generations of fermions, although familiar matter is formed
280 predominantly by the first generation. The generations are identical except for
281 their masses, which increase in each generation by convention. In addition, each
282 of these particles is accompanied by an antiparticle, with opposite-sign quantum
283 numbers but the same mass.

284 The fermions comprise what is typically considered matter, but there are
285 additional particles that are mediators of interactions between those fermions.
286 These mediators are known as the gauge bosons, gauge in that their existence
287 is required by gauge invariance (discussed further in Section 2.2) and bosons in
288 that they have integer spin. The boson which mediates the electromagnetic force
289 is the photon, the first boson to be discovered; it has no electric charge, no mass,
290 and a spin of 1. There are three spin-1 mediators of the weak force, the two W
291 bosons and the Z boson. The W bosons have electric charge of ± 1 and a mass of
292 80.385 ± 0.015 GeV, while the Z boson is neutral and has a mass of $91.1876 \pm$

293 0.0021 GeV. The strong force is mediated by eight particles called gluons, which
 294 are massless and electrically neutral but do carry color charge.

295 The final particle present in the SM is the Higgs boson, which was recently
 296 observed for the first time by experiments at CERN in 2012. It is electrically
 297 neutral, has a mass of 125.7 ± 0.4 GeV, and is the only spin-0 particle yet to be
 298 observed. The Higgs boson is the gauge boson associated with the mechanism
 299 that gives a mass to the W and Z bosons.

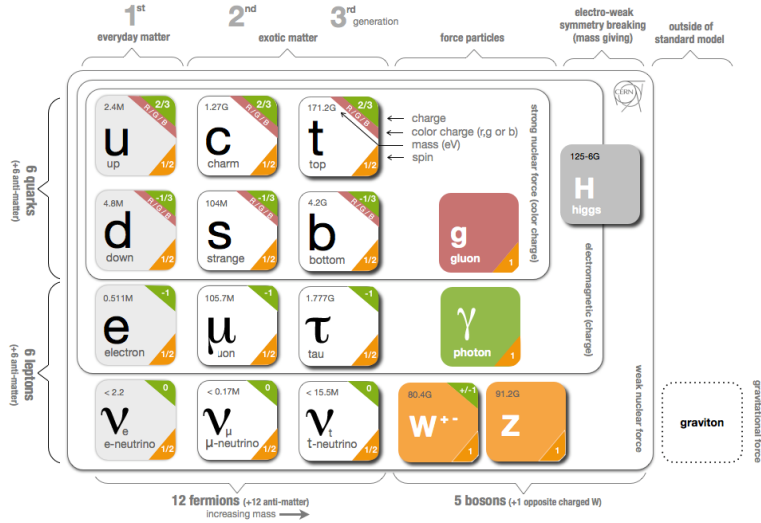


Figure 1: The particle content of the SM.

300 Together these particles form the entire content of the SM, and are summa-
 301 rized in Figure 1. These are the particles that constitute the observable universe
 302 and all the so-far-observed interactions within it.

303 2.2 INTERACTIONS

304 The interactions predicted and described by the SM are fundamentally tied to the
 305 particles within it, both in that they describe the way those particles can influence
 306 each other and also in that the existence of the interactions requires the existence
 307 of some particles (the gauge bosons).

308 2.3 LIMITATIONS

3

309

310 SUPERSYMMETRY

311 3.1 MOTIVATION

312 3.2 STRUCTURE

313 3.3 PHENOMENOLOGY

4

314

315 LONG-LIVED PARTICLES

316 4.1 MECHANISMS

317 4.1.1 EXAMPLES IN SUPERSYMMETRY

318 4.2 PHENOMENOLOGY

319 4.2.1 DISIMILARITIES TO PROMPT DECAYS

320 4.2.2 CHARACTERISTIC SIGNATURES

321

PART III

322

EXPERIMENTAL STRUCTURE AND RECONSTRUCTION

323

You can put some informational part preamble text here.

5

324

325 THE LARGE HADRON COLLIDER

326 5.1 INJECTION CHAIN

327 5.2 DESIGN AND PARAMETERS

328 5.3 LUMINOSITY

6

329

330 THE ATLAS DETECTOR

331 6.1 COORDINATE SYSTEM

332 6.2 MAGNETIC FIELD

333 6.3 INNER DETECTOR

334 6.3.1 PIXEL DETECTOR

335 6.3.2 SEMICONDUCTOR TRACKER

336 6.3.3 TRANSITION RADIATION TRACKER

337 6.4 CALORIMETRY

338 6.4.1 ELECTROMAGNETIC CALORIMETERS

339 6.4.2 HADRONIC CALORIMETERS

340 6.4.3 FORWARD CALORIMETERS

341 6.5 MUON SPECTROMETER

342 6.6 TRIGGER

343 6.6.1 TRIGGER SCHEME

344 6.6.2 MISSING TRANSVERSE ENERGY TRIGGERS

7

345

346 EVENT RECONSTRUCTION

347 The ATLAS experiment combines measurements in the subdetectors to form a
348 cohesive picture of each physics event.

349 7.1 TRACKS AND VERTICES

350 7.1.1 TRACK RECONSTRUCTION

351 7.1.1.1 NEURAL NETWORK

352 7.1.1.2 PIXEL DE/DX

353 7.1.2 VERTEX RECONSTRUCTION

354 7.2 JETS

355 7.2.1 TOPOLOGICAL CLUSTERING

356 7.2.2 JET ENERGY SCALE

357 7.2.3 JET ENERGY SCALE UNCERTAINTIES

358 7.2.4 JET ENERGY RESOLUTION

359 7.3 ELECTRONS

360 7.3.1 ELECTRON IDENTIFICATION

361 7.4 MUONS

362 7.4.1 MUON IDENTIFICATION

363 7.5 MISSING TRANSVERSE ENERGY

364

PART IV

365

CALORIMETER RESPONSE

366

You can put some informational part preamble text here.

369 As discussed in Section 7.2, colored particles produced in collisions hadronize
370 into jets of multiple hadrons. One approach to understanding jet physics in the
371 ATLAS calorimetry is to evaluate the calorimeter response to those individual
372 hadrons; measurements of individual hadrons can be used to build up an under-
373 standing of the jets that they form. The redundancy of the momentum provided
374 by the tracking system and the energy provided by the calorimeter provides an
375 opportunity to study calorimeter response using real collisions, as described fur-
376 ther in Section 8.2.

377 Calorimeter response includes a number of physical effects that can be ex-
378 tracted to provide insight into many aspects of jet modeling. First, many charged
379 hadrons interact with the material of the detector prior to reaching the calorime-
380 ters and thus do not deposit any energy. Comparing this effect in data and sim-
381 ulation is a powerful tool in validating the interactions of particles with the ma-
382 terial of the detector and the model of the detector geometry in simulation, see
383 Section 8.2.2. The particles which do reach the calorimeter deposit their energy
384 into individual cells, which are then clustered to measure full energy deposits.
385 Comparing the response in data to simulated hadrons provides a direct evalua-
386 tion of noise in the calorimeters, the showering of hadronic particles, and the
387 energy deposited by particles in matter (Section 8.2.4). These measurements are
388 extended to explore several additional effects, such as the dependence on charge,
389 in Section 8.2.4.1.

390 The above studies all use an inclusive selection of charged particles, which are
391 comprised predominantly of pions, kaons, and (anti)protons. It is also possible
392 to measure the particle types separately to evaluate the simulated interactions of
393 each particle, particularly at low energies where differences between species are
394 very relevant. Pions and (anti)protons can be identified through decays of long-
395 lived particles, in particular Λ , $\bar{\Lambda}$, and K_S^0 , and then used to measure response as
396 described above. This is discussed in detail in Section 8.3.

397 Together, these measurements in data provide a thorough understanding of
398 the way hadrons interact with the ATLAS detector and can be used to build up a
399 description of jets, as seen in Chapter 9. The results in this chapter use data col-
400 lected at 7 and 8 TeV collected in 2010 and 2012, respectively. Both are included
401 as the calorimeter was repaired and recalibrated between those two data-taking
402 periods. Both sets of data are compared to an updated simulation that includes
403 new physics models provided by Geant4 [12] and improvements in the detec-
404 tor description [2, 6]. These results are published in European Physical Journal
405 C (EPJC) [8] and can be compared to a similar measurement performed in 2009
406 and 2010 [5], which used the previous version of the simulation framework [1].

407 8.1 DATASET AND SIMULATION

408 8.1.1 DATA SAMPLES

409 The two datasets used in this chapter are taken from dedicated low-pileup runs
 410 where the fraction of events with multiple interactions was negligible, to facilitate
 411 measurement of isolated hadrons. The 2012 dataset at $\sqrt{s} = 8$ TeV contains
 412 8 million events and corresponds to an integrated luminosity of 0.1 nb^{-1} . The
 413 2010 dataset at $\sqrt{s} = 7$ TeV contains 3 million events and corresponds to an
 414 integrated luminosity of 3.2 nb^{-1} . The latter dataset was also used in the 2010
 415 results [5], but it has since been reanalyzed with an updated detector description
 416 for the material and alignment.

417 8.1.2 SIMULATED SAMPLES

418 The two datasets above are compared to simulated single-, double-, and non-
 419 diffractive events generated with Pythia8 [33] using the A2 configuration of
 420 hadronization [3] and the MSTW 2008 parton-distribution function set [28, 32].
 421 The conditions and energies for each run are matched in the two simulations.

422 To evaluate the interaction of hadrons with detector material, the simulation
 423 uses two different collections of hadronic physics models, called physics lists, in
 424 Geant4 9.4 [31]. The first, QGSP_BERT, combines the Bertini intra-nuclear
 425 cascade [17, 24, 26] below 9.9 GeV, a parametrized proton inelastic model from
 426 9.5 to 25 GeV [21], and a quark-gluon string model above 12 GeV [13, 14, 18, 19,
 427 22]. The second, FTFP_BERT, combines the Bertini intra-nuclear cascade [17, 24,
 428 26] below 5 GeV and the Fritiof model [15, 16, 23, 29] above 4 GeV. In either list,
 429 Geant4 enforces a smooth transition between models where multiple models
 430 overlap.

431 8.1.3 EVENT SELECTION

432 The event selection for this study is minimal, as the only requirement is selecting
 433 good-quality events with an isolated track. Such events are triggered by requiring
 434 at least two hits in the minimum-bias trigger scintillators. After trigger, each
 435 event is required to have exactly one reconstructed vertex, and that vertex is re-
 436 quired to have four or more associated tracks.

437 The particles which enter into the response measurements are first identified
 438 as tracks in the inner detector. The tracks are required to have at least 500 MeV
 439 of transverse momentum. To ensure a reliable momentum measurement, these
 440 tracks are required to have at least one hit in the pixel detector, six hits in the SCT,
 441 and small longitudinal and transverse impact parameters with respect to the pri-
 442 mary vertex [5]. For the majority of the measurements in this chapter, the track is
 443 additionally required to have 20 hits in the TRT, which significantly reduces the
 444 contribution from tracks which undergo nuclear interactions. This requirement
 445 and its effect is discussed in more detail in Section 8.2.4.1. In addition, tracks are
 446 rejected if there is another track which extrapolates to the calorimeter within a

⁴⁴⁷ cone of $\Delta R = \sqrt{(\Delta\phi)^2 + (\Delta\eta)^2} < 0.4$. This requirement guarantees that the
⁴⁴⁸ contamination of energy from nearby charged particles is negligible [5].

⁴⁴⁹ 8.2 INCLUSIVE HADRON RESPONSE

⁴⁵⁰ The calorimeter response is more precisely defined as the ratio of the measured
⁴⁵¹ calorimeter energy to the true energy carried by the particle, although this true
⁴⁵² energy is unknown. For charged particles, however, the inner detector provides
⁴⁵³ a very precise measurement of momentum (with uncertainty less than 1%) that
⁴⁵⁴ can be used as a proxy for true energy. The ratio of the energy deposited by the
⁴⁵⁵ charged particle in the calorimeter, E , to its momentum measured in the inner
⁴⁵⁶ detector p , forms the calorimeter response measure called E/p . Though the dis-
⁴⁵⁷tribution of E/p contains a number of physical features, this study focuses on
⁴⁵⁸ the trends in two aggregated quantities: $\langle E/p \rangle$, the average of E/p within a given
⁴⁵⁹ subset of particles, and the zero fraction, the fraction of particles with no associ-
⁴⁶⁰ated energy in the calorimeter.

⁴⁶¹ The calorimeter energy assigned to a track particle is defined using clusters.
⁴⁶² The clusters are formed using a 4–2–0 algorithm [9] that begins with seeds re-
⁴⁶³quiring at least 4 times the average calorimeter noise. The neighboring cells with
⁴⁶⁴at least twice that noise threshold are then added to the cluster, and all bound-
⁴⁶⁵ing cells are then added with no requirement. This algorithm minimizes noise
⁴⁶⁶contributions through its seeding process, and including the additional layers
⁴⁶⁷improves the energy resolution [34]. The clusters are associated to a given track
⁴⁶⁸if they fall within a cone of $\Delta R = 0.2$ of the extrapolated position of the track,
⁴⁶⁹which includes about 90% of the energy on average [5]. This construction is il-
⁴⁷⁰lustrated in Figure 2.

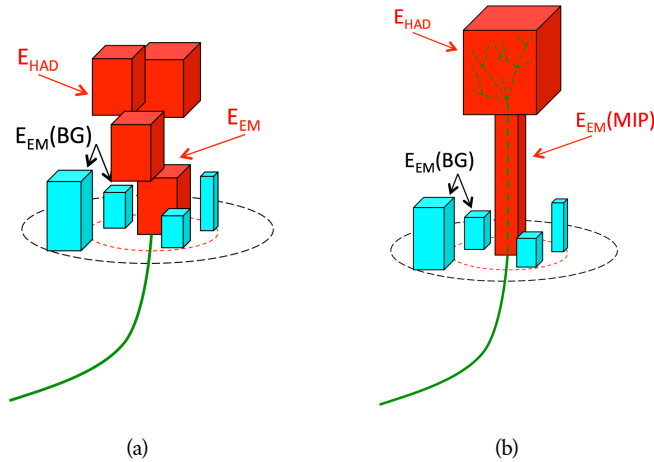


Figure 2: An illustration (a) of the E/p variable used throughout this paper. The red en-
ergy deposits come from the charged particle targeted for measurement, while
the blue energy deposits are from nearby neutral particles and must be sub-
tracted. The same diagram (b) for the neutral-background selection, described
in Section 8.2.3.

471 8.2.1 E/P DISTRIBUTION

472 The E/p distributions measured in both data and simulation are shown in Figure 3 for two example bins of track momentum and for tracks in the central
 473 region of the detector. These distributions show several important features of
 474 the E/p observable. The large content in the bin at $E = 0$ comes from tracks that
 475 have no associated cluster, which occurs due to interactions with detector mate-
 476 rial prior to reaching the calorimeter or the energy deposit being insufficiently
 477 large to generate a seed, and are discussed in Section 8.2.2. The small negative
 478 tail comes from similar tracks that do not deposit any energy in the calorime-
 479 ter but are randomly associated to a noise cluster. The long positive tail above
 480 1.0 comes from the contribution of neutral particles. Nearby neutral particles
 481 deposit (sometimes large) additional energy in the calorimeter but do not pro-
 482 duce tracks in the inner detector, so they cannot be rejected by the track isol-
 483 ation requirement. Additionally the peak and mean of the distribution falls below
 484 1.0 because of the loss of energy not found within the cone as well as the non-
 485 compensation of the calorimeter.
 486

487 The data and simulation share the same features, but the high and low tails
 488 are significantly different. The simulated events tend to overestimate the contri-
 489 bution of neutral particles to the long tail, an effect which can be isolated and
 490 removed as discussed in Section 8.2.3. Additionally, the simulated clusters have
 491 less noise on average, although this is a small effect on the overall response.

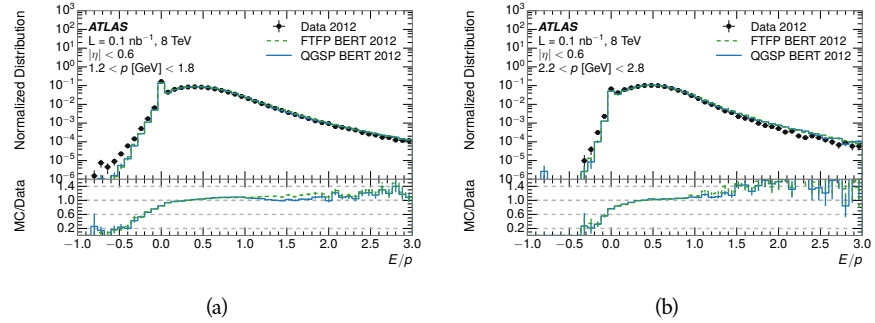


Figure 3: The E/p distribution and ratio of simulation to data for isolated tracks with
 (a) $|\eta| < 0.6$ and $1.2 < p/\text{GeV} < 1.8$ and (b) $|\eta| < 0.6$ and $2.2 < p/\text{GeV} < 2.8$.

492 8.2.2 ZERO FRACTION

493 The fraction of particles with no associated clusters, or similarly those with $E \leq$
 494 0, reflects the modeling of both the detector geometry and hadronic interactions.
 495 The zero fraction is expected to rise as the amount of material a particle traverses
 496 increases, while it is expected to decrease as the particle energy increases. This
 497 dependence can be seen in Figure 4, where the zero fraction in data and simula-
 498 tion is shown as a function of momentum and the amount of material measured
 499 in interaction lengths. The trends are similar between the 2010 and 2012 mea-
 500 surements. The zero fraction decreases with energy as expected. The amount of

material in the detector increases with η , which provides a distribution of interaction lengths. As the data and simulation have significant disagreement in the zero fraction over a number of interaction lengths, the difference must be primarily from the modeling of hadronic interactions with detector material and not just the detector geometry.

There is also a noticeable difference between positive and negative tracks at low momentum, which reflects the difference in response between protons and antiprotons. Antiprotons have significant model differences in the two physics lists, QGSP_BERT and FTFP_BERT, and this is evident in the lowest momentum bin of the data to simulation ratio. This difference is explored further in Section 8.3.

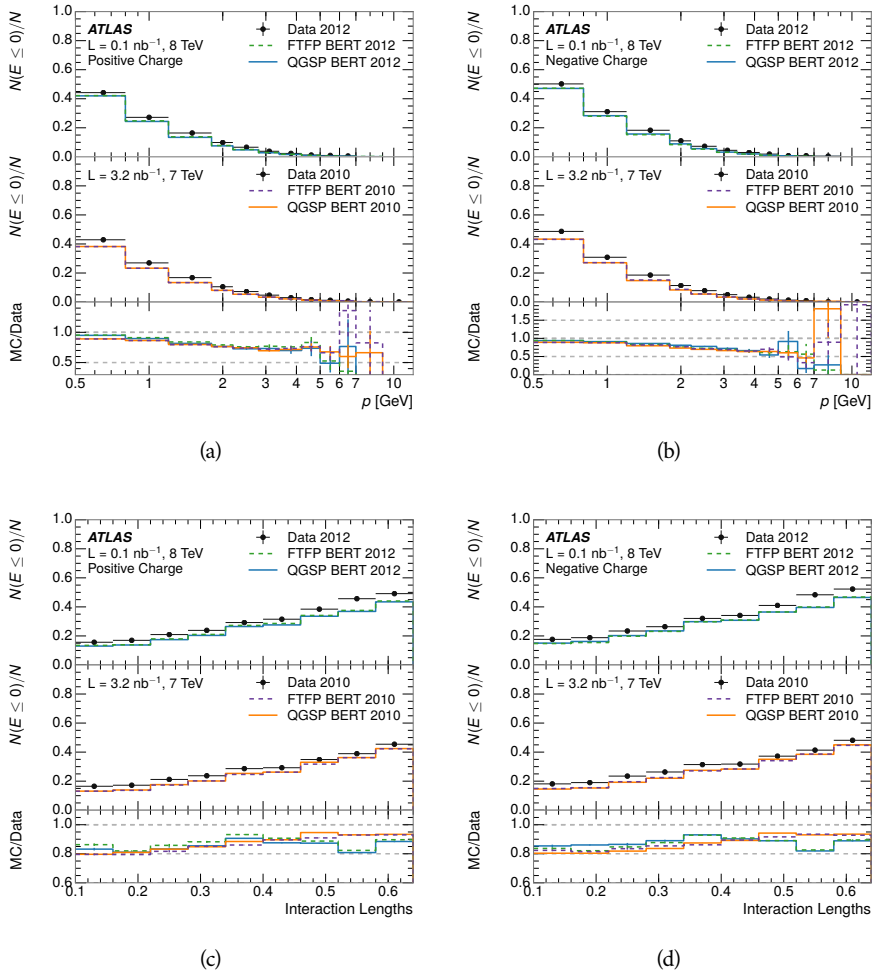


Figure 4: The fraction of tracks as a function (a, b) of momentum, (c, d) of interaction lengths with $E \leq 0$ for tracks with positive (on the left) and negative (on the right) charge.

512 8.2.3 NEUTRAL BACKGROUND SUBTRACTION

513 The isolation requirement on hadrons is only effective in remove energy contri-
 514 bution from nearby charged particles. Nearby neutral particles, predominantly
 515 photons from π^0 decays, also add their energy to the calorimeter clusters, but
 516 mostly in the electromagnetic calorimeter. It is possible to measure this contri-
 517 bution, on average, using late-showering hadrons that minimally ionize in the
 518 electromagnetic calorimeter. Such particles are selected by requiring that they
 519 deposit less than 1.1 GeV in the EM calorimeter within a cone of $\Delta R < 0.1$
 520 around the track. To ensure that these particles are well measured, they are addi-
 521 tionally required to deposit between 40% and 90% of their energy in the hadronic
 522 calorimeter within the same cone.

523 These particles provide a clean sample to measure the nearby neutral back-
 524 ground because they do not deposit energy in the area immediately surrounding
 525 them in the EM calorimeter, as shown in Figure 2. So, the energy deposits in the
 526 region $0.1 < \Delta R < 0.2$ can be attributed to neutral particles alone. To estimate
 527 the contribution to the whole cone considered for the response measurement,
 528 that energy is scaled by a geometric factor of 4/3. This quantity, $\langle E/p \rangle_{\text{BG}}$, mea-
 529 sured in aggregate over a number of particles, gives the contribution to $\langle E/p \rangle$
 530 from neutral particles in the EM calorimeter. Similar techniques were used in
 531 the individual layers of the hadronic calorimeters to show that the background
 532 from neutrals is negligible in those layers [5].

533 The distribution of this background estimate is shown in Figure 5. Although
 534 the simulation captures the overall trend, it significantly overestimates the neu-
 535 tral contribution for tracks with momentum between 2 and 8 GeV. This effect
 536 was also seen in the tails of the E/p distributions in Figure 3. This difference is
 537 likely due to the modeling of coherent neutral particle radiation in Pythia8, as
 538 the discrepancy does not depend on η and thus is unlikely to be a mismodeling
 539 of the detector. This difference can be subtracted to form a corrected average
 540 E/p , as in Section 8.2.4.

541 8.2.4 CORRECTED RESPONSE

542 Figure 6 shows $\langle E/p \rangle_{\text{COR}}$ as a function of momentum for several bins of pseu-
 543 dorapidity. This corrected $\langle E/p \rangle_{\text{COR}} \equiv \langle E/p \rangle - \langle E/p \rangle_{\text{BG}}$ measures the average
 544 calorimeter response without the contamination of neutral particles. It is the
 545 most direct measurement of calorimeter response in that it is the energy mea-
 546 sured for fully isolated hadrons. The correction is performed separately in data
 547 and simulation, so that the mismodeling of the neutral background in simulation
 548 is removed from the comparison of response. The simulation overestimates the
 549 response at low momentum by about 5%, an effect that can be mostly attributed
 550 to the underestimation of the zero fraction mentioned previously.

551 The response measurement above used topological clustering at the EM scale,
 552 that is clusters were formed to measure energy but no corrections were applied
 553 to correct for expected effects like energy lost outside of the cluster or in unin-
 554 strumented material. It is also interesting to measure $\langle E/p \rangle_{\text{COR}}$ using local clus-

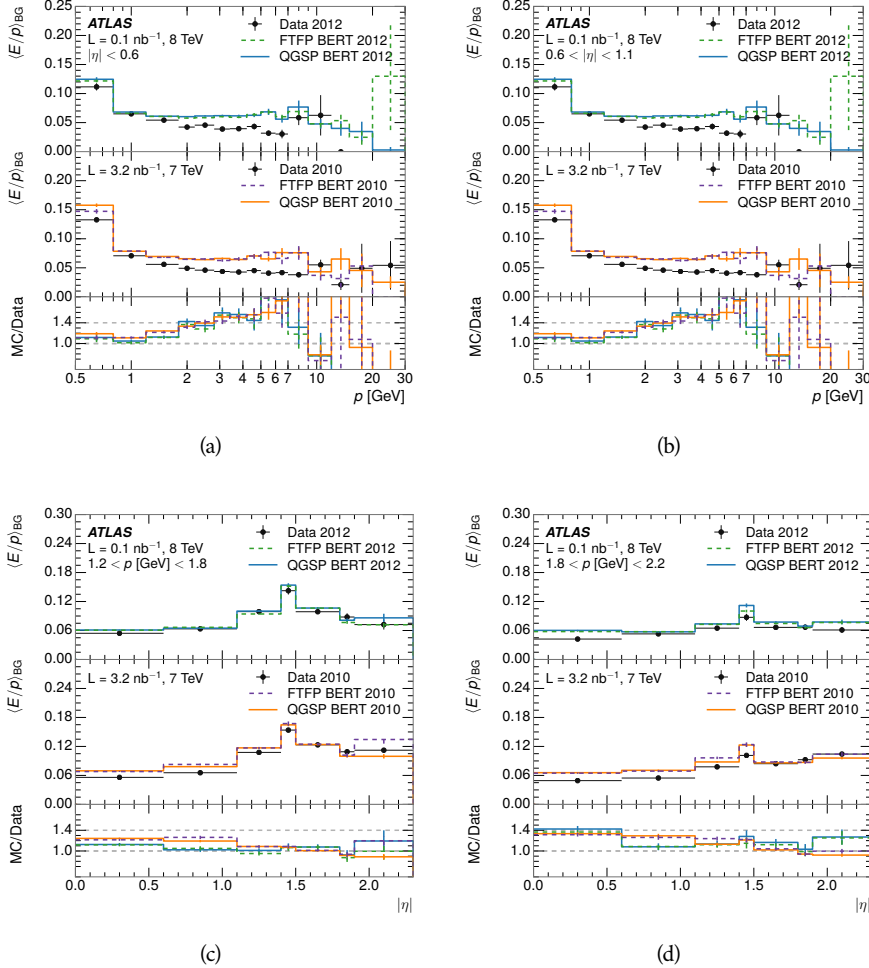


Figure 5: $\langle E/p \rangle_{\text{BG}}$ as a function of the track momentum for tracks with (a) $|\eta| < 0.6$, (b) $0.6 < |\eta| < 1.1$, and as a function of the track pseudorapidity for tracks with (c) $1.2 < p/\text{GeV} < 1.8$, (d) $1.8 < p/\text{GeV} < 2.2$.

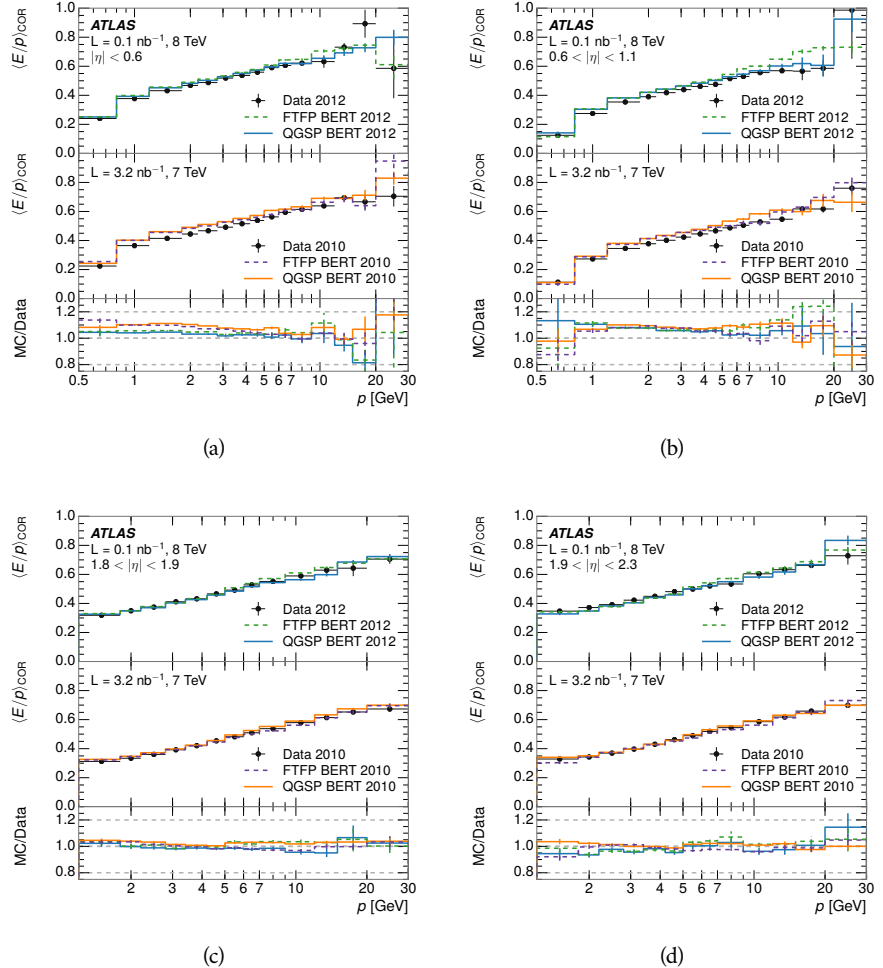


Figure 6: $\langle E/p \rangle_{\text{COR}}$ as a function of track momentum, for tracks with (a) $|\eta| < 0.6$, (b) $0.6 < |\eta| < 1.1$, (c) $1.8 < |\eta| < 1.9$, and (d) $1.9 < |\eta| < 2.3$.

555 ter weighted (LCW) energies, which accounts for those effects by calibrating the
 556 energy based on the properties of the cluster such as energy density and depth
 557 in the calorimeter. Figure 7 shows these distributions for tracks with zero or
 558 more clusters and separately for tracks with one or more clusters. The calibra-
 559 tion moves $\langle E/p \rangle_{\text{COR}}$ significantly closer to 1.0, which is the purpose of the cali-
 560 bration. The agreement between data and simulation improves noticeably when
 561 at least one cluster is required, as this removes the contribution from the mis-
 562 modeling of the zero fraction.

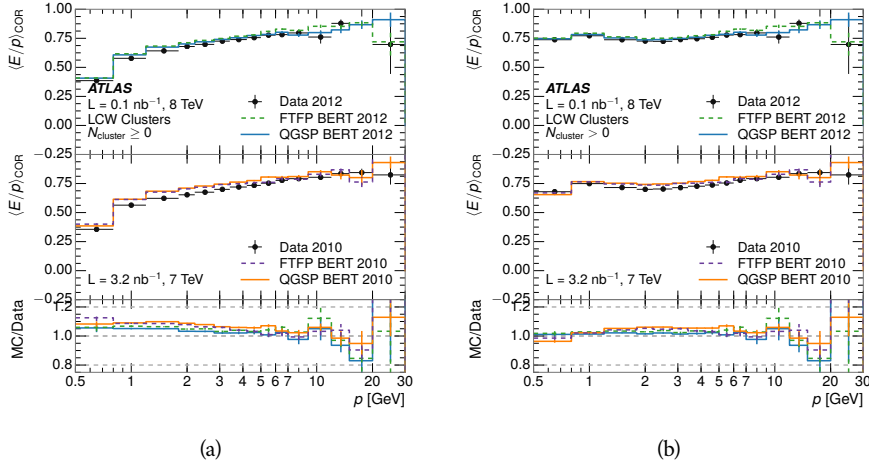


Figure 7: $\langle E/p \rangle_{\text{COR}}$ calculated using LCW-calibrated topological clusters as a function of track momentum for tracks with (a) zero or more associated topological clusters or (b) one or more associated topological clusters.

563 8.2.41 ADDITIONAL STUDIES

564 As has been seen in several previous measurements, the simulation does not
 565 correctly model the chance of a low momentum hadron to reach the calorime-
 566 ter. Because of the consistent discrepancy across pseudorapidity and interaction
 567 lengths, this seems to be best explained by incomplete understanding of hadronic
 568 interactions with the detector. For example, a hadron that scatters off of a nu-
 569 cleus in the inner detector can be deflected through a significant angle and not
 570 reach the expected location in the calorimeter. In addition, these interactions can
 571 produce secondary particles that are difficult to model.

572 The requirement on the number of hits in the TRT reduces these effects by
 573 preferentially selecting tracks that do not undergo nuclear interactions. It is inter-
 574 esting to check how well the simulation models tracks with low numbers of
 575 TRT hits, where the nuclear interactions are much more likely. Figure 8 com-
 576 pares the distributions with $N_{\text{TRT}} < 20$ to $N_{\text{TRT}} > 20$ for real and simulated
 577 particles. As expected, the tracks with fewer hits are poorly modeled in the sim-
 578 ulation as $\langle E/p \rangle_{\text{COR}}$ differs by as much as 25% at low momentum.

579 Another interesting aspect of the simulation is the description of antiprotons
 580 at low momentum, where QGSP_BERT and FTFP_BERT have significant differ-
 581 ences. This can be seen to have an effect in the inclusive response measurement

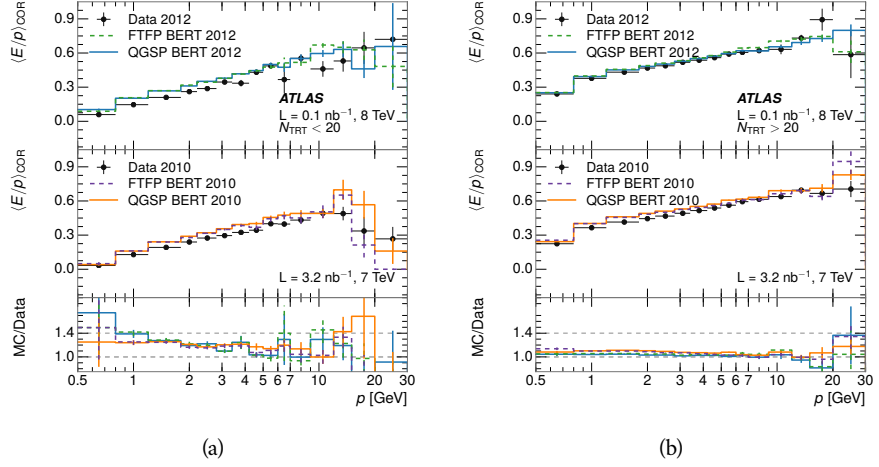


Figure 8: Comparison of the $\langle E/p \rangle_{\text{COR}}$ for tracks with (a) less than and (b) greater than 20 hits in the TRT.

when separated into positive and negative charge. The $\langle E/p \rangle_{\text{COR}}$ distributions for positive and negative particles are shown in Figure 9, where a small difference between QGSP_BERT and FTFP_BERT can be seen in the distribution for negative tracks. This is demonstrated more clearly in Figure 10, which shows the E/p distribution in the two simulations separated by charge. There is a clear difference around $E/p > 1.0$, which can be explained by the additional energy deposited by the annihilation of the antiproton in the calorimeter that is modeled well only in FTFP_BERT. This is also explored with data using identified antiprotons in Section 8.3.

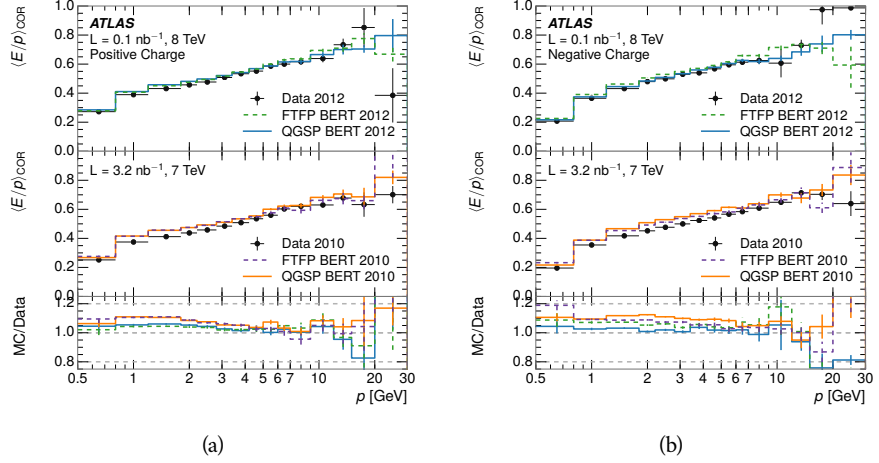


Figure 9: Comparison of the $\langle E/p \rangle_{\text{COR}}$ for (a) positive and (b) negative tracks as a function of track momentum for tracks with $|\eta| < 0.6$.

The $\langle E/p \rangle$ results in previous sections have considered the electromagnetic and hadronic calorimeters together as a single energy measurement, to emphasize the total energy deposited for a given particle. However, the deposits in each

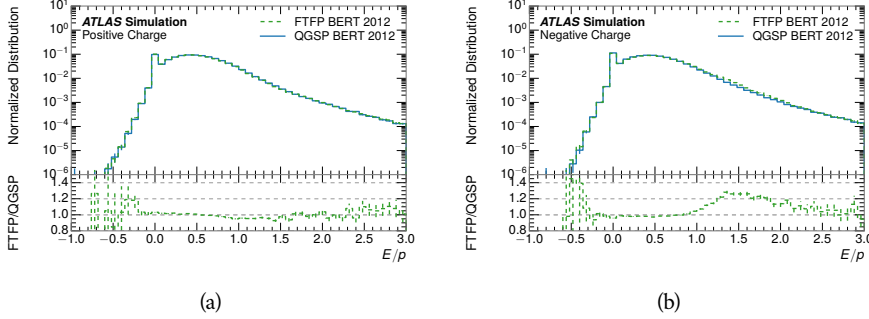


Figure 10: Comparison of the E/p distributions for (a) positive and (b) negative tracks with $0.8 < p/\text{GeV} < 1.2$ and $|\eta| < 0.6$, in simulation with the FTFP_BERT and QGSP_BERT physics lists.

calorimeter are available separately and $\langle E/p \rangle$ can be constructed for each layer. As the layers are composed of different materials and are modeled separately in the detector geometry, confirmation that the simulation matches the data well in each layer adds confidence in both the description of hadronic interactions with the two different materials and also the geometric description of each.

The technique discussed in Section 8.2.3 for selecting minimally ionizing particle (**MIP**s) in the electromagnetic calorimeter is also useful in studying deposits in the hadronic calorimeter. Those **MIP**s deposit almost all of their energy exclusively in the hadronic calorimeter. Figure 11 shows $\langle E/p \rangle_{\text{RAW}}^{\text{Had}}$, where RAW indicates that no correction has been applied for neutral backgrounds and Had indicates that only clusters for the hadronic calorimeter are included. The RAW and COR versions of $\langle E/p \rangle$ in this case are the same, as the neutral background is negligible in that calorimeter layer. The distributions are shown both for the original EM scale calibration and after LCW calibration. The data and simulation agree very well in this comparison, except in the lowest momentum bin which has 5% discrepancy that has already been seen in similar measurements.

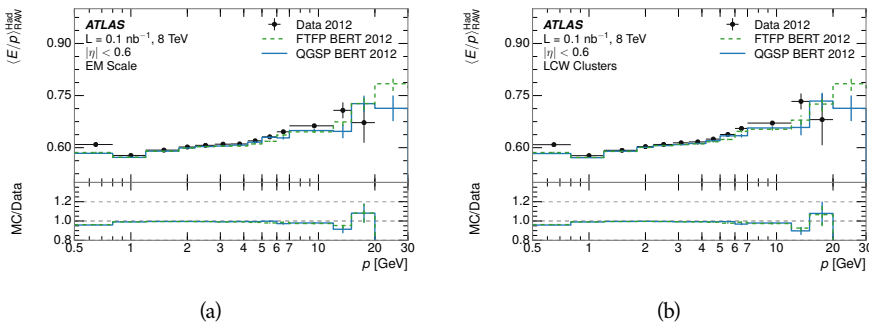


Figure 11: Comparison of the response of the hadronic calorimeter as a function of track momentum (a) at the EM-scale and (b) after the LCW calibration.

A similar comparison can be made in the electromagnetic calorimeter by selecting particles which have no associated energy in the hadronic calorimeter. These results are measured in terms of $\langle E/p \rangle_{\text{COR}}^{\text{EM}}$, where EM designates that

613 only clusters in the electromagnetic calorimeter are included and COR designates that the neutral background is subtracted as the neutral background is
 614 present in this case. Figure 12 shows the analogous comparisons to Figure 11 in
 615 the electromagnetic calorimeter. In this case the disagreement between data and
 616 simulation is more pronounced, with discrepancies as high as 5% over a larger
 617 range of momenta. This level of discrepancy indicates that the description of the
 618 electromagnetic calorimeter is actually the dominant source of discrepancy in
 619 the combined distributions in Section 8.2.4.
 620

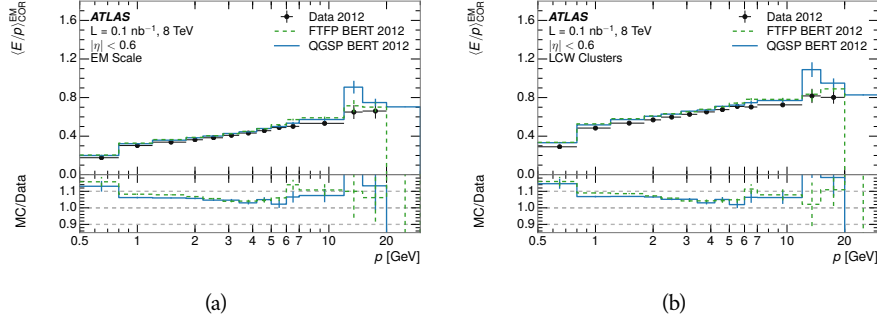


Figure 12: Comparison of the response of the EM calorimeter as a function of track momentum (a) at the EM-scale and (b) with the LCW calibration.

621 **NOTE: There are more studies that I skipped for brevity that could be**
 622 **included if interesting. E/p at different cluster threshold settings, E/p with**
 623 **pileup, E/p with cells. I also left out a lot of eta bins that appear in the paper**
 624 **so that this section didn't turn into 20 pages of plots.**

625 8.3 IDENTIFIED PARTICLE RESPONSE

626 The inclusive response measurement for hadrons can be augmented by measuring
 627 the response for specific particle species. The simulation models each parti-
 628 cle type separately, and understanding the properties of each is important in con-
 629 straining the uncertainty on jets. In order to select and measure specific hadrons,
 630 this section relies on the displaced decays of long-lived particles. Such decays can
 631 be identified by reconstructing secondary vertices with a requirement on mass.
 632 In particular, Λ , $\bar{\Lambda}$, and K_S^0 can be used to select a pure sample of protons, an-
 633 tiprotons, and pions, respectively.

634 8.3.1 DECAY RECONSTRUCTION

635 The measurement of response for identified particles uses the same selection
 636 as for inclusive particles (Section 8.1.3) with a few additions. Each event used
 637 is required to have at least one secondary vertex, and the tracks are required
 638 to match to that vertex rather than the primary vertex. Pions are selected from
 639 decays of $K_S^0 \rightarrow \pi^+ \pi^-$, which is the dominant decay for K_S^0 to charged particles.
 640 Protons are selected from decays of $\Lambda \rightarrow \pi^- p$ and antiprotons from $\bar{\Lambda} \rightarrow \pi^+ \bar{p}$,

which are similarly the dominant decays of Λ and $\bar{\Lambda}$ to charged particles. The species of parent hadron in these decays is determined by reconstructing the mass of the tracks associated to the secondary vertex. The sign of the higher momentum decay particle can distinguish between Λ and $\bar{\Lambda}$, which of course have the same mass, as the proton or antiproton is kinematically favored to have higher momentum. Examples of the reconstructed masses used to select these decays are shown in Figure 13.

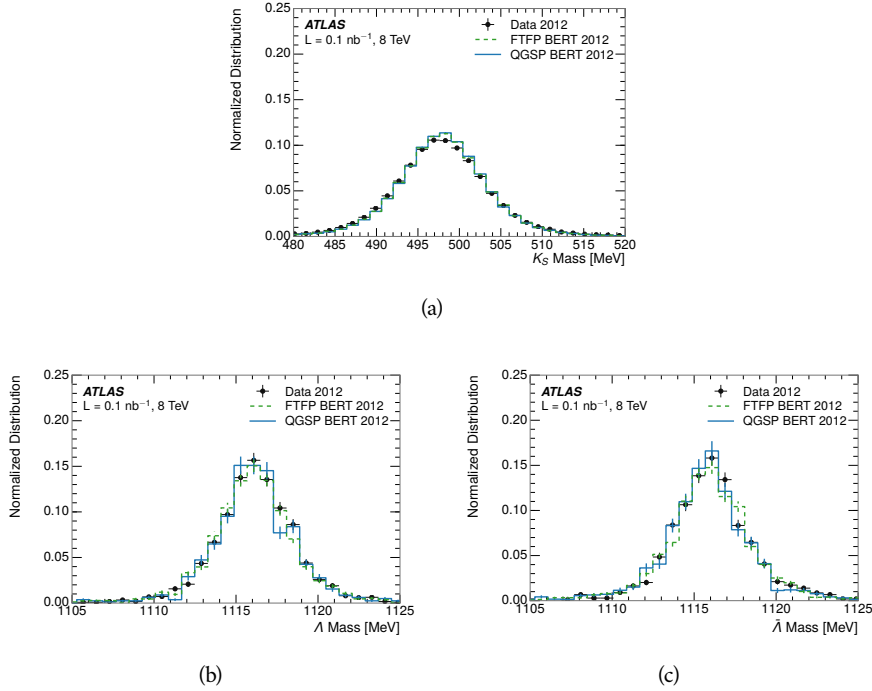


Figure 13: The reconstructed mass peaks of (a) K_S^0 , (b) Λ , and (c) $\bar{\Lambda}$ candidates.

The dominant backgrounds for the identified particle decays are nuclear interactions and combinatoric sources. These are suppressed by the kinematic requirements on the tracks as well as an additional veto which removes candidates that are consistent with both a Λ or $\bar{\Lambda}$ and a K_S^0 hypothesis, which is possible because of the different assumptions on particle mass in each case [5]. After these requirements, the backgrounds are found to be negligible compared to the statistical errors on these measurements.

8.3.2 IDENTIFIED RESPONSE

With these techniques the E/p distributions are extracted in data and simulation for each particle species and shown in Figure 14. These distributions are shown for a particular bin of E_a ($2.2 < E_a/\text{GeV} < 2.8$), rather than p . E_a is the energy available to be deposited in the calorimeter: for pions $E_a = \sqrt{p^2 + m^2}$, for protons $E_a = \sqrt{p^2 + m^2} - m$, and for antiprotons $E_a = \sqrt{p^2 + m^2} + m$. The features of the E/p distributions are similar to the inclusive case. There is a small negative tail from noise and a large fraction of tracks with zero energy from particles which do not reach the calorimeter. The long positive tail is noticeably more

664 pronounced for antiprotons because of the additional energy generated by the
 665 annihilation in addition to the neutral background.

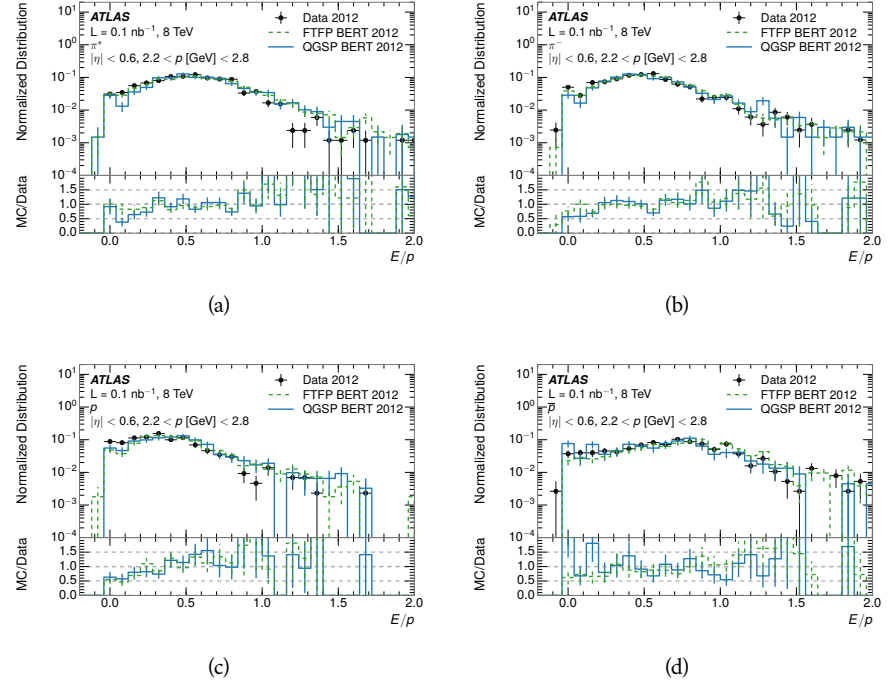


Figure 14: The E/p distribution for isolated (a) π^+ , (b) π^- , (c) proton, and (d) anti-proton tracks.

666 The zero fraction is further explored in Figure 15 for pions and protons in
 667 data and simulation. The simulation consistently underestimates the zero frac-
 668 tion independent of particle species, which implies that this discrepancy is not
 669 caused by the model of a particular species but rather a feature common to all.

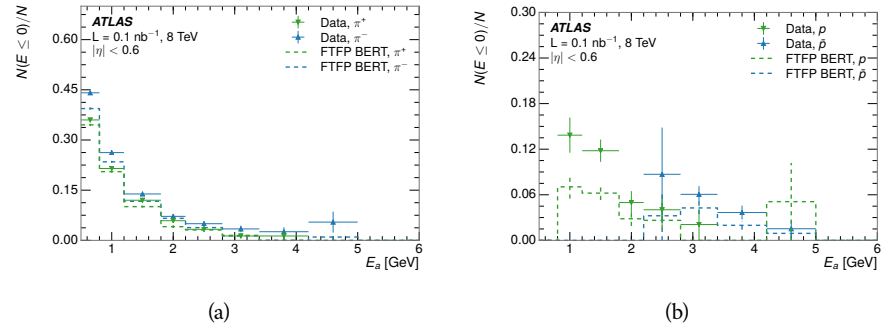


Figure 15: The fraction of tracks with $E \leq 0$ for identified (a) π^+ and π^- , and (b) proton and anti-proton tracks

670 It is also interesting to compare the response between the different particle
 671 species. One approach to do this is to measure the difference in $\langle E/p \rangle$ between
 672 two types, which has the advantage of removing the neutral background. These
 673 differences are shown in various combinations in Figure 16. The response for

π^+ is greater on average than the response to π^- because of a charge-exchange effect which causes the production of additional neutral pions in the showers of π^+ [20]. The response for π^+ is also greater on average than the response to p , because a large fraction of the energy of π^+ hadrons is converted to an electromagnetic shower [11, 25]. However, the \bar{p} response is significantly higher than the response to π^- because of the annihilation of the antiproton. FTFP_BERT does a better job of modeling this effect than QGSP_BERT because of their different descriptions of \bar{p} interactions with material.

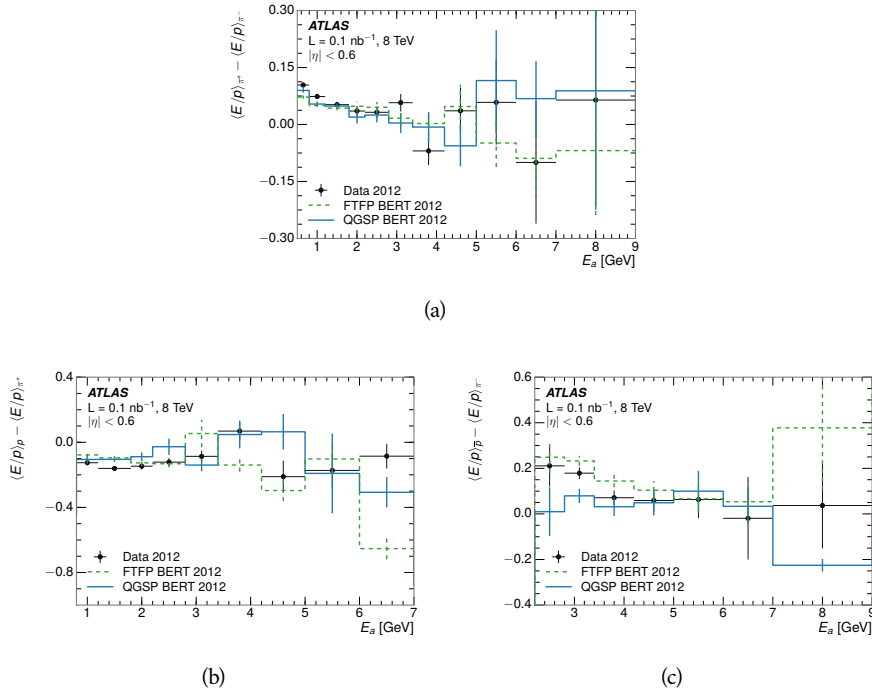


Figure 16: The difference in $\langle E/p \rangle$ between (a) π^+ and π^- (b) p and π^+ , and (c) \bar{p} and π^- .

It is also possible to remove the neutral background from these response distributions using the same technique as in Section 8.2.3. The technique is largely independent of the particle species and so can be directly applied to $\langle E/p \rangle$ for pions. The $\langle E/p \rangle_{\text{COR}}$ distributions for pions are shown in Figure 17, which are very similar to the inclusive results. The inclusive hadrons are comprised mostly of pions, so this similarity is not surprising. It is also possible to see the small differences between π^+ and π^- response here, where $\langle E/p \rangle_{\text{COR}}$ is higher on average for π^+ . The agreement between data and simulation is significantly worse for the π^- distributions than for the π^+ , with a discrepancy greater than 10% below 2-3 GeV.

8.3.3 ADDITIONAL SPECIES IN SIMULATION

The techniques above provide a method to measure the response separately for only pions and protons. However the hadrons which forms jets include a number of additional species such as kaons and neutrons. The charged kaons are

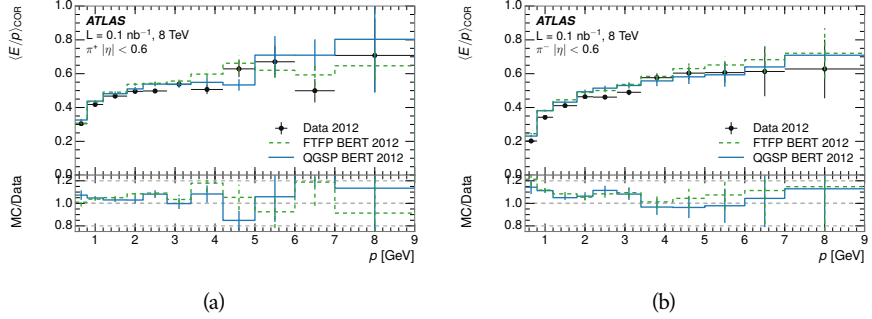


Figure 17: $\langle E/p \rangle_{\text{COR}}$ as a function of track momentum for (a) π^+ tracks and (b) π^- tracks.

an important component of the inclusive charged hadron distribution, which is comprised of roughly 60-70% pions, 15-20% kaons, and 5-15% protons. These are difficult to measure in data at the ATLAS detector, although a template subtraction technique has been proposed which may be effective with larger sample sizes [8]. The simulation of these particles includes noticeable differences in response at low energies, which are shown in Figure 18 for FTFP_BERT. The significant differences in response between low energy protons and antiprotons are accounted for above in the definitions of E_a .

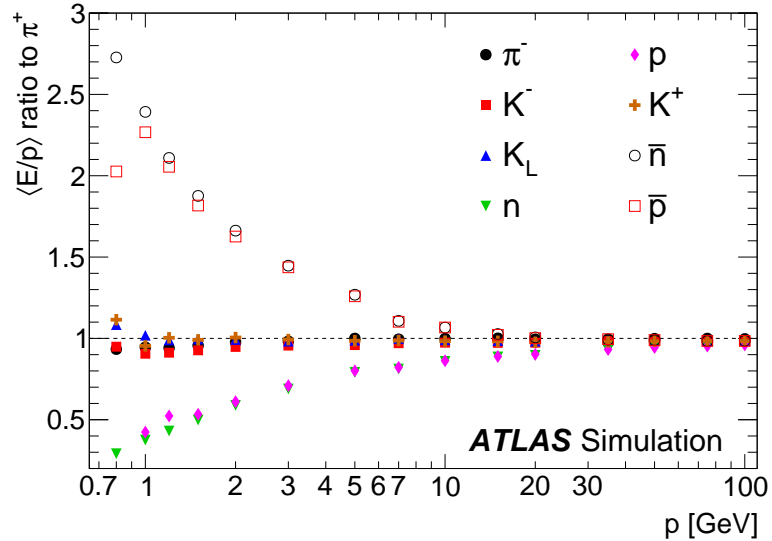


Figure 18: The ratio of the calorimeter response to single particles of various species to the calorimeter response to π^+ with the physics list FTFP_BERT.

8.4 SUMMARY

These various measurements of calorimeter response shown above for data and simulation illuminate the accuracy of the simulation of hadronic interactions at the ATLAS detector. The results were done using 2010 and 2012 data at 7 and 8

708 TeV, but reflect the most current understanding of the detector alignment and
709 geometry. A number of measurements focusing on a comparison between pro-
710 tons and antiprotons suggest that FTFP_BERT models those interaction more
711 accurately than QGSP_BERT. These measurements, among others, were the moti-
712 vation to switch the default Geant4 simulation from FTFP_BERT to QGSP_BERT
713 for all ATLAS samples.

714 Even with these updates, there are a number of small, approximately 5%, dis-
715 crepancies in response between the data and simulation at low energies. At higher
716 energies the simulation of hadronic interactions is very consistent with data.
717 Chapter 9 discusses how to use these observed differences to constrain the jet
718 energy scale and its associated uncertainties.

719

720 JET ENERGY RESPONSE AND UNCERTAINTY

721 9.1 MOTIVATION

722 As jets form a major component of many physics analyses at ATLAS, it is cru-
 723 cial to carefully calibrate the measurement of jet energies and to derive an un-
 724 certainty on that measurement. These uncertainties have often been the domi-
 725 nant systematic uncertainty in high-energy analyses at the Large Hadron Col-
 726 llider ([LHC](#)). Dijet and multijet balance techniques provide a method to constrain
 727 the [JES](#) and its uncertainty in data, and provide the default values used for ATLAS
 728 jet measurements at most energies [7]. These techniques are limited by their re-
 729 liance on measuring jets in data, so they are statistically limited in estimating
 730 the jet energy scale at the highest jet energies. This chapter presents another
 731 method for estimating the jet energy scale and its uncertainty which builds up a
 732 jet from its components and thus can be naturally extended to high jet momen-
 733 tum. Throughout this chapter the jets studied are simulated using [Pythia8](#) with
 734 the CT10 parton distribution set [27] and the AU2 tune [3], and corrections are
 735 taken from the studies including data and simulation in Chapter 8.

736 As described in Section 7.2, jets are formed from topological clusters of energy
 737 in the calorimeters using the anti- k_t algorithm. These clusters originate from a
 738 diverse spectrum of particles, in terms of both species and momentum, leading to
 739 significantly varied jet properties and response between jets of similar produced
 740 momentum. Figure 19 shows the simulated distribution of particles within jets
 741 at a few examples energies. The E/p measurements provide a thorough under-
 742 standing of the dominant particle content of jets, the charged hadrons.

743 9.2 UNCERTAINTY ESTIMATE

744 Simulated jets are not necessarily expected to correctly model the energy de-
 745 posits in the calorimeters, because of the various discrepancies discussed in Chap-
 746 ter 8. To evaluate a jet energy response, the simulated jet energies are compared
 747 to a corrected jet built up at the particle level. Each cluster in a jet is associated
 748 to the truth particle which deposited it, and the energy in that cluster is then
 749 corrected for a number of effects based on measurements in data. The primary
 750 corrections come from the single hadron response measurements in addition to
 751 response measured using the combined test beam which covers higher momen-
 752 tum particles [10]. These corrections include both a shift (Δ), in order to make the
 753 simulation match the average response in data, and an uncertainty (σ) associated
 754 with the ability to constrain the difference between data and simulation. Some of
 755 the dominant sources of uncertainty are itemized in Table ?? with typical values,
 756 and the full list considered is described in detail in the associated paper [8]. These

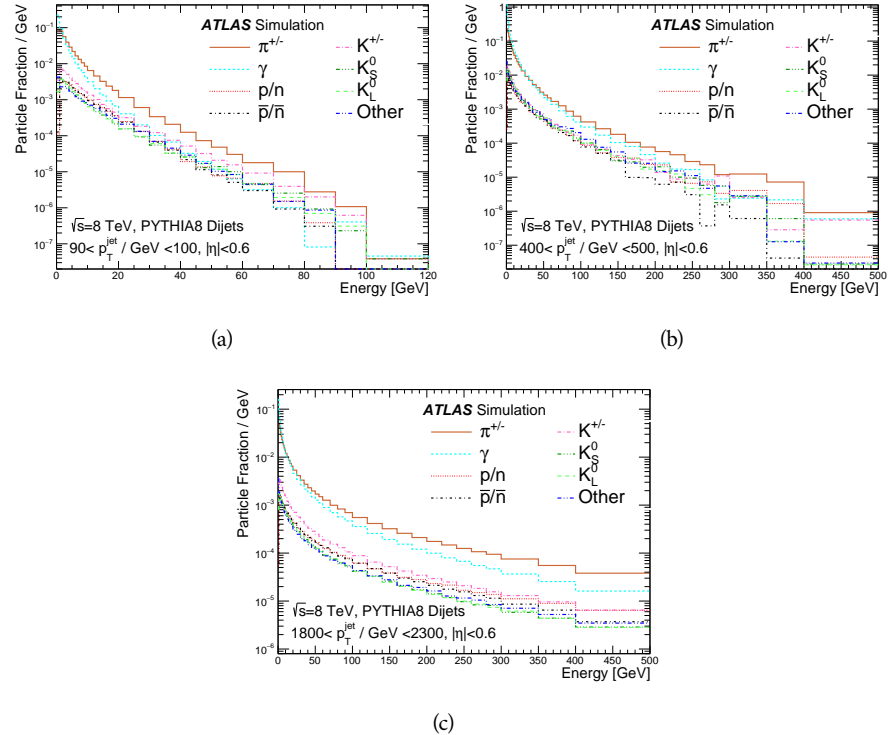


Figure 19: The spectra of true particles inside anti- k_t , $R = 0.4$ jets with (a) $90 < p_T/\text{GeV} < 100$, (b) $400 < p_T/\text{GeV} < 500$, and (c) $1800 < p_T/\text{GeV} < 2300$.

757 uncertainties cover differences between the data and simulation in the modeling
 758 of calorimeter response to a given particle. No uncertainties are added for the
 759 difference between particle composition of jets in data and simulation.

760 From these terms, the jet energy scale and uncertainty is built up from individual energy deposits in simulation. Each uncertainty term is treated independently, and are taken to be gaussian distributed. The resulting scale and uncertainty is shown in Figure 20, where the mean response is measured relative to the calibrated energy reported by simulation. The dominant uncertainties come from the statistical uncertainties on the E/p measurements at lower energies and the additional uncertainty for out of range measurements at higher energies. The total uncertainty from this method at intermediate jet energies is comparable to other simulation-based methods [4] and is about twice as large as in-situ methods using data [7]. This method is the only one which provides an estimation above 1.8 TeV, however, and so is still a crucial technique in analyses that search for very energetic jets.

772 These techniques can also be used to measure the correlation between bins of average reconstructed jet momentum across a range of p_T and $|\eta|$, where correlations are expected because of a similarity in particle composition at similar 773 energies. Figure 21 shows these correlations, where the uncertainties on jets in 774 neighboring bins are typically between 30% and 60% correlated. The uncertainty 775 on all jets becomes significantly correlated at high energies and larger pseudora- 776
 777

Abbrev.	Description	Δ (%)	σ (%)
In situ E/p	The comparison of $\langle E/p \rangle_{\text{COR}}$ as described in Chapter 8 with statistical uncertainties from 500 MeV to 20 GeV.	0-3	1-5
CTB	The main $\langle E/p \rangle$ comparison uncertainties, binned in p and $ \eta $, as derived from the combined test beam results, from 20 to 350 GeV [10].	0-3	1-5
E/p Zero Fraction	The difference in the zero-fraction between data and MC simulation from 500 MeV to 20 GeV.	5-25	1-5
E/p Threshold	The uncertainty in the EM calorimeter response from the potential mismodeling of threshold effects in topological clustering.	0	0-10
Neutral	The uncertainty in the calorimeter response to neutral hadrons based on studies of physics model variations.	0	5-10
K_L	An additional uncertainty in the response to neutral K_L in the calorimeter based on studies of physics model variations.	0	20
E/p Misalignment	The uncertainty in the p measurement from misalignment of the ID.	0	1
Hadrons, $p > 350$ GeV	A flat uncertainty for all particles above the energy range or outside the longitudinal range probed with the combined test beam.	0	10

Table 1: The dominant sources of corrections and systematic uncertainties in the [JES](#) estimation technique, including typical values for the correcting shift (Δ) and the associated uncertainty (σ).

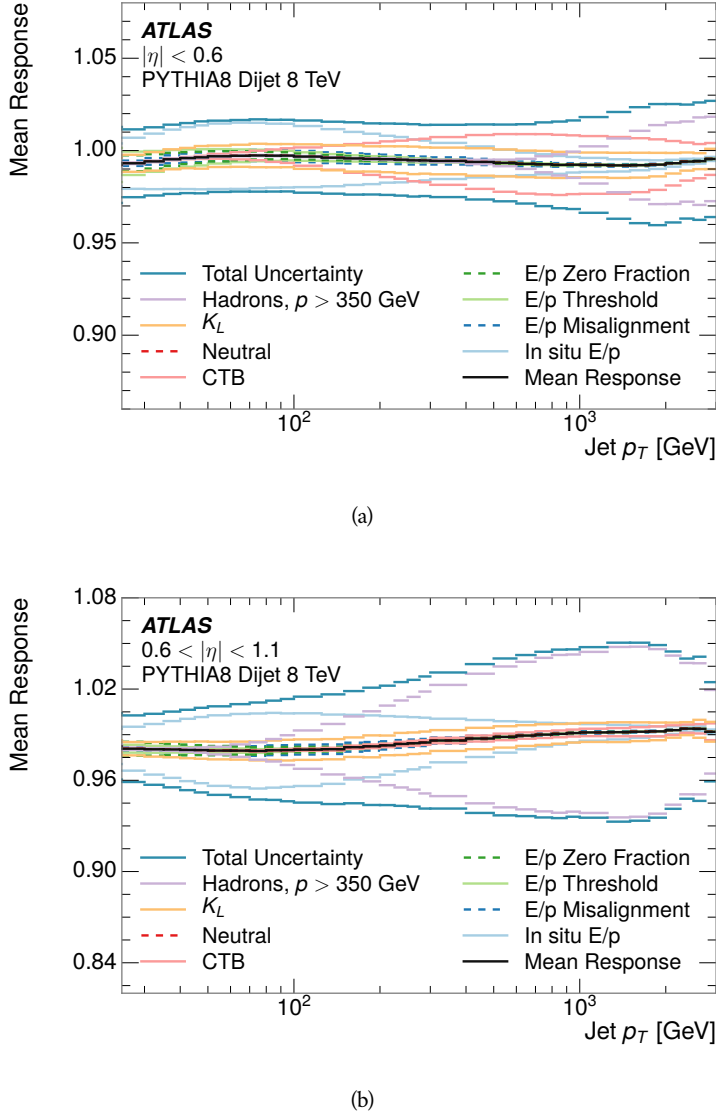


Figure 20: The [JES](#) uncertainty contributions, as well as the total [JES](#) uncertainty, as a function of jet p_T for (a) $|\eta| < 0.6$ and (b) $0.6 < |\eta| < 1.1$.

778 pidities, when the uncertainty becomes dominated by the single term reflecting
 779 out of range particles.

780 9.3 SUMMARY

781 The technique described above provides a jet energy scale and uncertainty by
 782 building up jet corrections from the energy deposits of constituent particles. The
 783 E/p measurements are crucial in providing corrections for the majority of parti-
 784 cles in the jets. The uncertainty derived this way is between 2 and 5% and is about
 785 twice as large at corresponding momentum than jet balance methods. However
 786 this is the only uncertainty available for very energetic jets using 2012 data and
 787 simulation, and repeating this method with Run 2 data and simulation will be

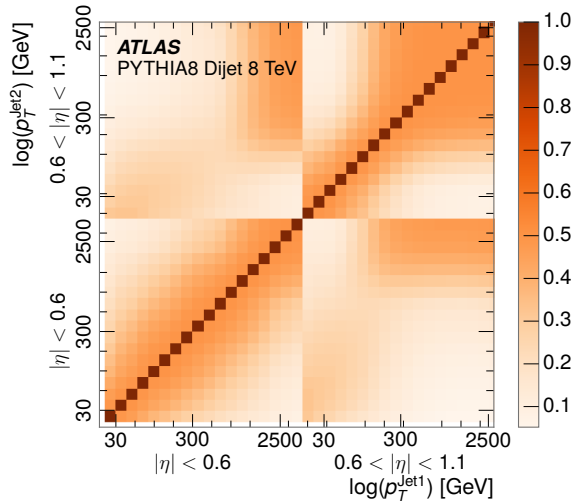


Figure 21: The JES correlations as a function of jet p_T and $|\eta|$ for jets in the central region of the detector.

788 important in providing an uncertainty for the most energetic jets in 13 TeV col-
 789 lisions.

790

PART V

791

SEARCH FOR LONG-LIVED PARTICLES

792

You can put some informational part preamble text here.

10

793

794 LONG-LIVED PARTICLES IN ATLAS

795 10.1 OVERVIEW AND CHARACTERISTICS

796 10.2 SIMULATION

798 EVENT SELECTION

799 The Long-Lived Particles ([LLPs](#)) targeted by this search differ in their interactions
 800 with the detector from [SM](#) particles primarily because of their large mass. When
 801 produced at the energies available at the [LHC](#), that large mass results in a low β
 802 and such slow-moving particles heavily ionize in detector material. Each layer
 803 of the pixel detector provides a measurement of that ionization, through time
 804 over threshold ([ToT](#)), as discussed in Section [6.3.1](#). The ionization in the pixel
 805 detector, quantified in terms of dE/dx , provides the major focus for this search
 806 technique, both for its discriminating power and also because of the large range
 807 of lifetimes where it can be used. The dE/dx variable needs to be augmented
 808 with a few additional selection requirements to form a complete search.

809 Ionization is not currently available in any form during triggering, so this
 810 search instead relies on E_T^{miss} to trigger signal events. Although triggering on
 811 E_T^{miss} is not particularly efficient, E_T^{miss} is often large for many production mech-
 812 anisms of [LLPs](#), as discussed in Section [10.1](#).

813 Ionization is most effective in rejecting backgrounds for well-measured, high-
 814 momentum tracks, so some basic requirements on quality and kinematics are
 815 placed on the particles considered in this search. In particular a newly introduced
 816 tracking variable is very effective in removing highly-ionizing backgrounds caused
 817 by overlapping tracks. A few additional requirements are placed on the tracks
 818 considered for [LLP](#) candidates that increase background rejection by targeting
 819 specific types of [SM](#) particles. These techniques provide a significant analysis
 820 improvement over previous iterations of ionization-based searches on ATLAS
 821 by providing additional background rejection with minimal loss in signal effi-
 822 ciency.

823 The ionization measurement with the Pixel detector can be calibrated to pro-
 824 vide an estimator of $\beta\gamma$. That estimate, together with the momentum measure-
 825 ment provided by tracking, can be used to reconstruct a mass for each track
 826 which traverses the pixel detector. That mass variable will be peaked at the [LLP](#)
 827 mass for any signal, and provides an additional tool to search for an excess. In
 828 addition to an explicit requirement on ionization, this search constructs a mass-
 829 window for each targeted mass range in order to evaluate any excess of events
 830 and to set limits.

831 The strategy discussed here is optimized for lifetimes of $O(1) - O(10)$ ns.
 832 Pixel ionization is especially useful in this regime as particles only need to prop-
 833 agate through the first seven layers of the inner detector, about 37 cm from the
 834 beam axis. The search is still competitive with other searches for [LLPs](#) at longer
 835 lifetimes, because the primary discriminating variables are still applicable even
 836 for particles that do not decay within the detector. Although the basic strategy
 837 remains the same for all lifetimes, two signal regions are defined to optimize
 838 separately for intermediate and long lifetime particles.

839 11.1 TRIGGER

840 Triggering remains one of the primary difficulties in defining an event selection
 841 with high signal efficiency in a search for **LLPs**. There are no triggers available in
 842 the current ATLAS system that can fire directly from a high momentum track
 843 with large ionization (Section 6.6). Although in some configurations a charged
 844 **LLP** can fire muon triggers, this requirement introduces significant model depen-
 845 dence on both the allowed lifetimes and the interactions in the calorimeter.

846 For a search targeting particles which may decay prior to reaching the muon
 847 system, the most efficient available trigger is based on missing energy. As dis-
 848 cussed in Section 10.1, signal events can produce E_T^{miss} by two primary mech-
 849 anisms. The decays of R-Hadrons to neutralinos can produce missing energy
 850 when the neutralinos go undetected in the calorimeters. **LLPs** which do not de-
 851 cay before the calorimeters also can produce missing energy because they do
 852 not deposit much energy. Either case to some extent relies on kinematic degrees
 853 of freedom to produce missing energy, as the pair-produced **LLPs** tend to bal-
 854 ance each other in the transverse plane. That balance results in a relatively low
 855 efficiency for long-lifetime particles, roughly 40%, and efficiencies between 65%
 856 and 95% for shorter lifetimes depending on both the mass and the lifetime.

857 11.2 KINEMATICS AND ISOLATION

858 After the trigger requirement, each event is required to have a primary vertex
 859 reconstructed from at least two well-measured tracks in the inner detector, each
 860 with $p_T > 400$ MeV. If more than one such vertex exists, the primary vertex is
 861 taken to be the one with the largest summed track momentum for all tracks as-
 862 sociated to that vertex. The offline reconstructed E_T^{miss} is required to be above
 863 130 GeV to additionally reject **SM** backgrounds. The transverse missing energy
 864 is calculated using fully reconstructed and calibrated offline objects, as described
 865 in Section 7.5. In particular the E_T^{miss} definition in this selection uses jets recon-
 866 structed with the anti- k_t algorithm with radius $R = 0.4$ from clusters of energy
 867 in the calorimeter (Section 7.2) and with $p_T > 20$ GeV, as well as reconstructed
 868 muons, electrons, and tracks not identified as another object type.

869 The E_T^{miss} distributions are shown for data and a few simulated signals in Fig-
 870 ure 22, after the trigger requirement. The cut placed at 130 GeV is 95% efficient
 871 for metastable and 90% efficient for stable particles, because of the missing en-
 872 ergy generating mechanisms discussed previously. The distribution of data in
 873 this figure and subsequent figures in this section can be interpreted as the dis-
 874 tribution of backgrounds, as any signal contamination would be negligible if
 875 present at these early stages of the selection (prior to the final requirement on
 876 mass). The background falls rapidly with missing energy, motivating the direct
 877 requirement on E_T^{miss} for the signal region. Although a tighter requirement than
 878 the specified value of 130 GeV would seem to increase the search potential from
 879 these early distributions, other requirements are more optimal when taken as a
 880 whole. The specific values for each requirement in signal region were optimized
 881 considering the increase in discovery reach for tightening the requirement on

882 each discriminating variable. **NOTE: Is it interesting to discuss the signal re-
 883 gion optimization process in detail? I could add another section on how
 884 the values were determined, although in truth it is at least partially his-
 885 torical precedence.**

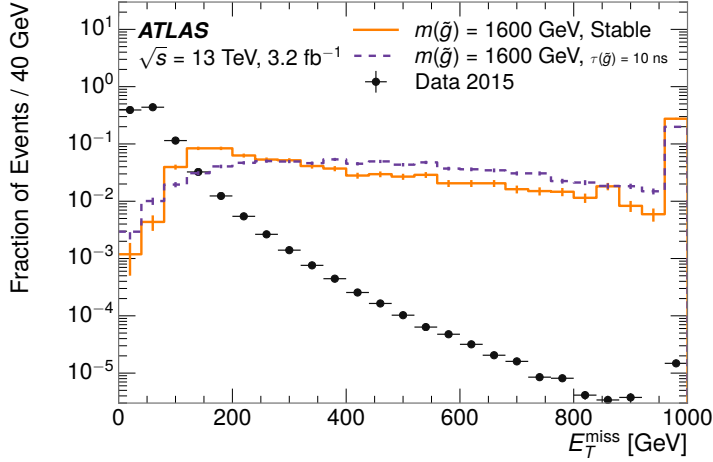


Figure 22: The distribution of E_T^{miss} for data and simulated signal events, after the trigger requirement.

886 Potential signal events are then required to have at least one candidate LLP
 887 track. Although the LLPs are produced in pairs, many models do not consistently
 888 yield two charged particles. For example, in the R-Hadron model highlighted
 889 here, only 20% of events have two charged R-Hadrons while 47% of events have
 890 just one. A signal region requiring two charged candidates could be a powerful
 891 improvement in background rejection for a larger dataset, but it is not consid-
 892 ered in this version of the analysis as it was found to be unnecessary to reject the
 893 majority of backgrounds.

894 For a track to be selected as a candidate, it must have $p_T > 50 \text{ GeV}$ and pass
 895 basic quality requirements. The track must be associated to the primary vertex. It
 896 must also have at least seven clusters in the silicon layers in the inner detector to
 897 ensure an accurate measurement of momentum. Those clusters must include one
 898 in the innermost layer if the extrapolated track is expected to pass through that
 899 layer. And to ensure a reliable measurement of ionization, the track is required
 900 to have at least two clusters in the pixel detector that provide a measurement of
 901 dE/dx .

902 At this point in the selection, there is a significant high-ionization background
 903 from multiple tracks that significantly overlap in the inner detector. Previous
 904 version of this analysis have rejected these overlaps by an explicit overlap rejec-
 905 tion between pairs of fully reconstructed tracks, typically by requiring no addi-
 906 tional tracks within a cone around the candidate. This technique, however, fails
 907 to remove the background from tracks that overlap so precisely that the tracks
 908 cannot be separately resolved.

909 A new method, added in Run 2, identifies cluster shapes that are likely formed
 910 by multiple tracks based on a neural network classification algorithm. The num-

911 number of clusters that are classified this way in the pixel detector for a given track
 912 is called N_{split} . As the shape of clusters requires significantly less spatial sepa-
 913 ration to identify overlaps than it does to reconstruct two fully resolved tracks,
 914 this variable is more effective at rejecting backgrounds from overlaps. Figure 23
 915 shows the dependence of ionization on N_{split} ; as N_{split} increases the mean of
 916 dE/dx grows significantly up to twice the expected value when $N_{\text{split}} = 4$.

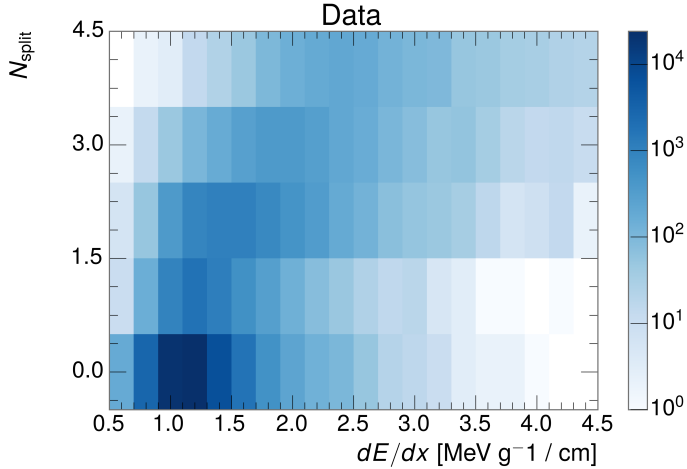


Figure 23: The dependence of dE/dx on N_{split} in data after basic track hit requirements have been applied.

917 This requirement is very successful in reducing the long positive tail of the
 918 dE/dx distributions, as can be seen in Figure 24. Comparing the distribution for
 919 “baseline tracks”, tracks with only the above requirements on clusters applied and
 920 before the requirement on N_{split} , to the distribution with $N_{\text{split}} = 0$, it is clear
 921 that the fraction of tracks with large dE/dx is reduced by several orders of mag-
 922 nitude. The isolated tracks are very close to the dE/dx distribution of identified
 923 muons, which are extremely well isolated on average. Figure 24 also includes
 924 the distribution of dE/dx in an example signal simulation to demonstrate how
 925 effective dE/dx is as a discriminating variable with this isolation applied. The
 926 background falls rapidly for $dE/dx > 1.8 \text{ MeVg}^{-1}\text{cm}^2$ while the majority of
 927 the signal, approximately 90% depending on the mass, falls above that threshold.
 928 Over 90% of LLP tracks in simulated signal events pass the N_{split} -based isolation
 929 requirement.

930 A few additional kinematic requirements are imposed to help reduce SM back-
 931 grounds. The momentum of the candidate track must be at least 150 GeV, and
 932 the uncertainty on that measurement must be less than 50%. The distribution of
 933 momentum is shown in Figure 25 for tracks in data and simulated signal events
 934 after the previously discussed requirements on clusters, transverse momentum,
 935 and isolation have been imposed. The signal particles are much harder on aver-
 936 age than their backgrounds because of the high energy interactions required to
 937 produce them. The transverse mass, m_T , defined as

$$m_T = \sqrt{2 p_T E_T^{\text{miss}} (1 - \cos(\Delta\phi(E_T^{\text{miss}}, \text{track})))} \quad (1)$$

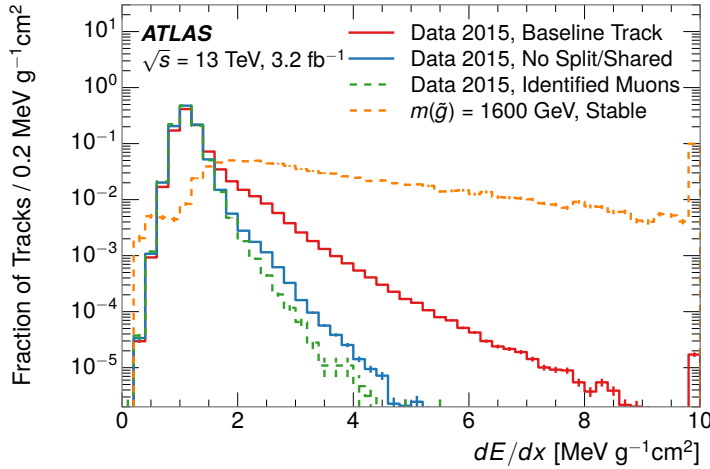


Figure 24: The distribution of dE/dx with various selections applied in data and simulated signal events.

estimates the mass of a decay of to a single charged particle and an undetected particle and is required to be greater than 130 GeV to reject contributions from the decay of W bosons. Figure 26 shows the distribution of m_T for data and simulated signal events. The signal is distributed over a wide range of m_T , with about 90% above the threshold value of 130 GeV. The data shows a dual-peaked structure, where the first peak comes from W boson decays and the second peak is a kinematic shaping from the requirements on E_T^{miss} and the track p_T in dijet events.

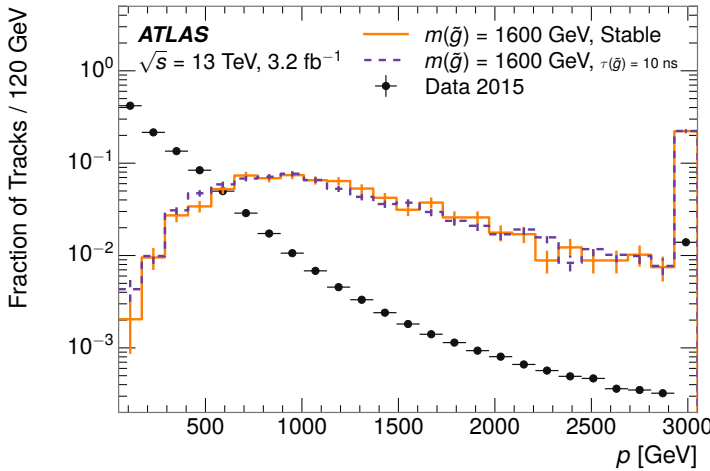


Figure 25: The distribution of track momentum for data and simulated signal events, after previous selection requirements have been applied.

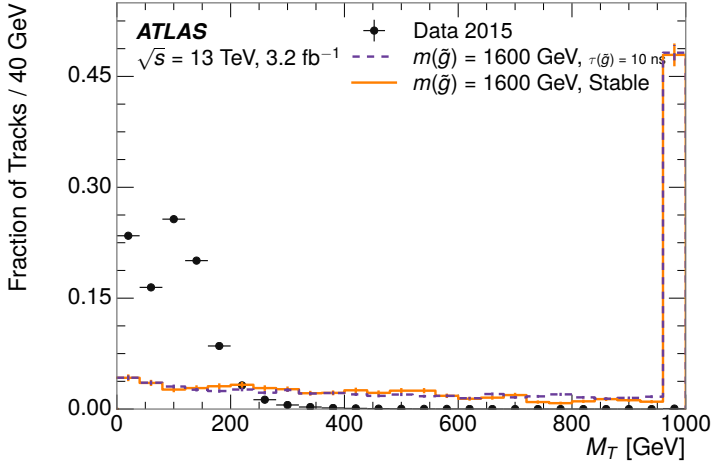


Figure 26: The distribution of M_T for data and simulated signal events, after previous selection requirements have been applied.

946 11.3 STANDARD MODEL REJECTION

947 Because the search selects events with just a single, highly-ionizing track, back-
 948 grounds can be formed by a wide variety of SM processes when various charged
 949 particles have a few randomly large deposits of energy in the pixel detector. Those
 950 backgrounds can be effectively rejected by targeting the types of particles pro-
 951 duced rather than the processes which produce them, as LLPs will have signifi-
 952 cant differences compared to any SM particle. These rejections focus on using
 953 additional features of the event, other than the kinematics or ionization of the
 954 candidate track, as it provides a powerful source of background rejection with
 955 very high signal efficiency. The lifetime of the particle can significantly change
 956 its detector characteristics, as discussed in Section 10.1. To accomodate these
 957 differences, the SM rejections defined in this section are split to form two signal
 958 regions, one for long-lifetimes particles, the “stable” region, and one for interme-
 959 diate lifetime particles, the “metastable” region.

960 Jets can be very effectively rejected by considering the larger-scale isolation of
 961 the candidate track. In this case the isolation focuses on the production of nearby
 962 particles as a jet-veto, rather than isolation from overlapping tracks to reduce
 963 high-ionization backgrounds. As explained in Section 10.1, the fragmentation
 964 process which produces an R-Hadron is very hard and thus is not expected to
 965 produce additional particles. The jet-veto uses the summed momentum of tracks
 966 with a cone of $\Delta R < 0.25$, referred to as p_T^{Cone} , which is shown in Figure 27
 967 for data and simulated signal events. In the data this value has a peak at zero
 968 from isolated tracks such as leptons, and a long tail from jets which contains as
 969 much as 80% of the background above 20 GeV at this stage of the selection. In
 970 signal events p_T^{Cone} is strongly peaked at zero and significantly less than 1% is
 971 above 20 GeV. This makes a requirement of $p_T^{\text{Cone}} < 20$ GeV one of the most
 972 effective methods to reject background without losing signal efficiency. For the

stable signal region, this cut is further tightened to $p_T^{\text{Cone}} < 5 \text{ GeV}$ as it is the most effective variable remaining to extend the search reach for long lifetimes.

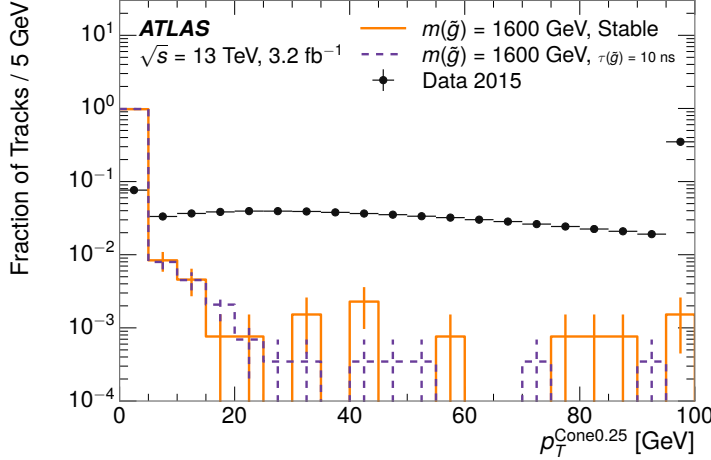


Figure 27: The distribution of summed tracked momentum within a cone of $\Delta R < 0.25$ around the candidate track for data and simulated signal events, after previous selection requirements have been applied.

Even for fully isolated particles, there are additional methods to reject each type of particle using information in the muon system and calorimeters. Muons can be identified very reliably using the tracks in the muon system, as described in Section 7.4. For intermediate lifetimes the LLPs do not survive long enough to reach the muon system, and so muons are vetoed by rejecting tracks that associate to a muon with medium muon identification requirements. For longer lifetimes, this rejection is not applied because LLPs which reach the muon system can be identified as muons as often as 30% of the time in simulated samples.

Calorimeter-based particle rejection relies on the expected small deposits of energy from LLPs. When the lifetime is long enough to reach the calorimeter, a LLP deposits little of its energy as it traverses the material, as discussed in Section 10.1. Even when the particle does decay before the calorimeter, the majority of its energy is carried away by the Lightest Supersymmetric Particle (LSP) and not deposited in the calorimeter. In both cases the energy is expected to be distributed across the layers of the calorimeters and not peaked in just one layer. This can be quantified in terms of E/p , the ratio of calorimeter energy of a nearby jet to the track momentum, and f_{EM} , the fraction of energy in that jet within the electromagnetic calorimeter. When no jets fall within a cone of 0.05 of the particle, E/p and f_{EM} are both defined as zero. E/p is expected to be above 1.0 for typical SM particles because of calibration and the contributions from other nearby particles. At these momenta there is no significant zero fraction due to interactions with the detector or insufficient energy deposits (see Section 8.2.2). f_{EM} is peaked close to 1.0 for electrons, and distributed between 10% and 90% for hadrons.

These trends can be seen in the two dimensional distribution for signal in Figure 28 for stable and metastable (10 ns) events. The majority of R-Hadrons in

1001 both samples fall into the bin for $E/p = 0$ and $f_{\text{EM}} = 0$ because the majority of
 1002 the time there is no associated jet. In the stable sample, when there is an associ-
 1003 ated jet, E/p is typically still below 0.1, and the f_{EM} is predominantly under 0.8.
 1004 In the metastable sample, on the other hand, E/p is larger but still typically below
 1005 0.1 because of actual jets produced during the decay. The f_{EM} is much lower on
 1006 average in this case, below 0.1, because the 10 ns lifetime particles rarely decay
 1007 before passing through the electromagnetic calorimeter. Figure 28 also includes
 1008 simulated Z decays to electrons or tau leptons. From the decays to electrons it is
 1009 clear that the majority of electrons have f_{EM} above 0.9. The tau decays include a
 1010 variety of products. Muons can be seen in the bin where $E/p = 0$ and $f_{\text{EM}} = 0$
 1011 because they do not have an associated jet. Electrons fall into the range where
 1012 $E/p > 1$ and $f_{\text{EM}} > 0.9$. Hadronic tau decays are the most common, and fall in
 1013 the range of $0.1 < f_{\text{EM}} < 0.9$ and $E/p > 1.0$.

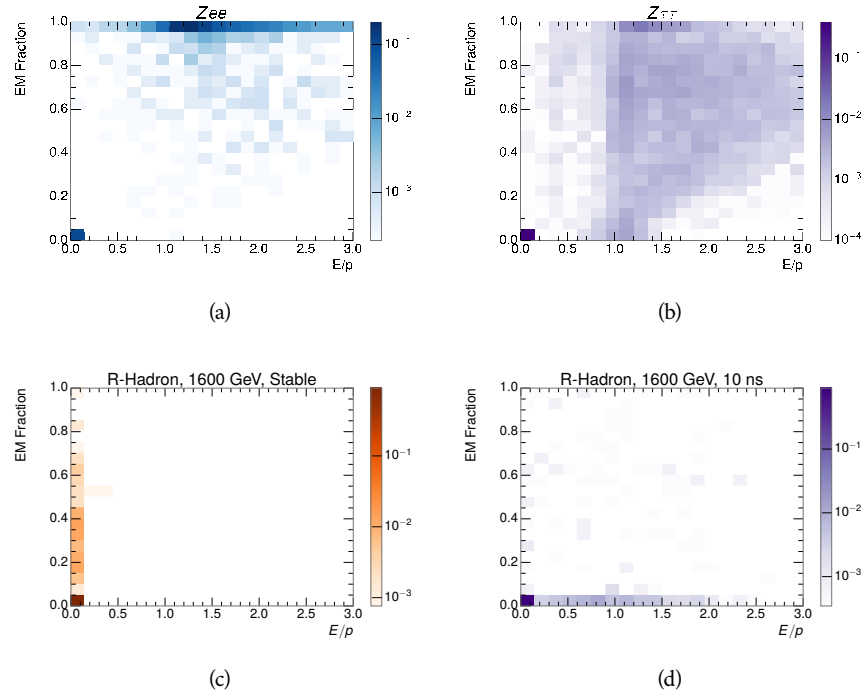


Figure 28: The normalized, two-dimensional distribution of E/p and f_{EM} for simulated
 (a) $Z \rightarrow ee$, (b) $Z \rightarrow \tau\tau$, (c) 1200 GeV Stable R-Hadron events, and (d) 1200
 GeV, 10 ns R-Hadron events.

1014 These differences motivate an electron rejection by requiring an f_{EM} below
 1015 0.9. Similarly, isolated hadrons are rejected by requiring $E/p < 1.0$. These re-
 1016 quirements combine to remove the majority of isolated electrons and hadrons
 1017 but retain over 95% of the simulated signal across a range of masses and lifetimes.

11.4 IONIZATION

1019 The final requirements on the candidate track are the primary discriminating
 1020 variables, the ionization in the pixel detector and the corresponding mass. That

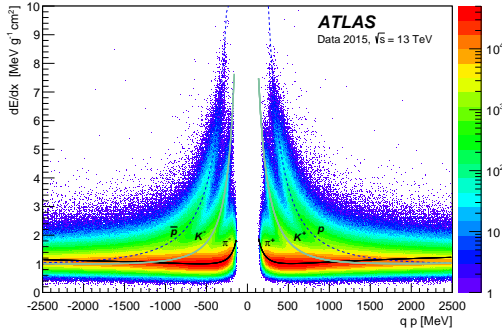


Figure 29: Two-dimensional distribution of dE/dx versus charge signed momentum (qp) for minimum-bias tracks. The fitted distributions of the most probable values for pions, kaons and protons are superimposed.

ionization is measured in terms of dE/dx , which was shown for data and simulated signal events in Figure 24. dE/dx is dramatically greater for the high mass signal particles than the backgrounds, which start to fall immediately after the minimally ionizing peak at $1.1 \text{ MeVg}^{-1} \text{ cm}^2$. The dE/dx for candidate tracks must be greater than a pseudorapidity-dependent threshold, specifically $1.80 - 0.11|\eta| + 0.17\eta^2 - 0.05|\eta|^3 \text{ MeV g}^{-1} \text{ cm}^{-2}$, in order to correct for an approximately 5% dependence of the MIP peak on η . The requirement was chosen as part of the signal region optimization, and manages to reduce the backgrounds by a factor of 100 while remaining 70-90% efficient for simulated signal events depending on the mass.

1031 11.4.1 MASS ESTIMATION

1032 The mean value of ionization in silicon is governed by the Bethe-Bloch formula
 1033 and the most probable value follows a Landau-Vavilov distribution [30]. Those
 1034 forms inspire a parametric description of dE/dx in terms of $\beta\gamma$,

$$(dE/dx)_{\text{MPV}}(\beta\gamma) = \frac{p_1}{\beta^{p_3}} \ln(1 + [p_2\beta\gamma]^{p_5}) - p_4 \quad (2)$$

1035 which performs well in the range $0.3 < \beta\gamma < 1.5$. This range includes the ex-
 1036 pected range of $\beta\gamma$ for the particles targeted for this search, with $\beta\gamma \approx 2.0$
 1037 for lower mass particles ($O(100 \text{ GeV})$) and up to $\beta\gamma \approx 0.5$ for higher mass par-
 1038 ticles ($O(1000 \text{ GeV})$). The parameters, p_i , are fit using a 2015 data sample of low-
 1039 momentum pions, kaons, and protons as described in Ref. [ATLAS-CONF-2011-016].
 1040 Figure 29 shows the two-dimensional distribution of dE/dx and momentum
 1041 along with the above fitted values for $(dE/dx)_{\text{MPV}}$.

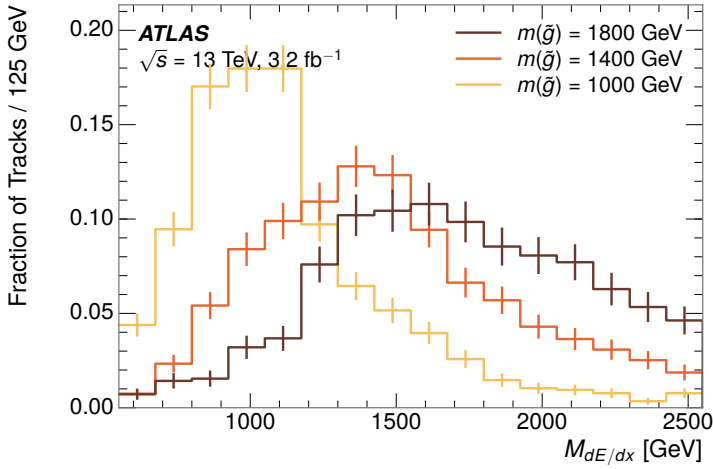


Figure 30: The distribution of mass estimated using dE/dx for simulated stable R-Hadrons with masses between 1000 and 1600 GeV.

1042 The above equation (2) is then numerically inverted to estimate $\beta\gamma$ and then
 1043 mass for each candidate track. In simulated signal events, the mean of this mass
 1044 value reproduces the generated mass up to around 1800 GeV to within 3%, and
 1045 3% shift is applied to correct for this difference. The mass distributions prior to
 1046 this correction are shown for a few stable mass points in Figure 30. The large
 1047 widths of these distributions come from the high variability in energy deposits
 1048 in the pixel detector, but the means converge to the expected values.

1049 This analysis evaluates expected yields and the resulting cross sectional limits
 1050 using windows in this mass variable. The windows are formed by fitting mass
 1051 distributions like those in Figure 30 to Gaussian distribution and taking all events
 1052 that fall within $\pm 1.4\sigma$ of the mean. As can be seen in Figure 30, typical values for
 1053 this width are $\sigma \approx 300 - 500$ GeV depending on the generated mass.

1054 11.5 SUMMARY

1055 The numbers of events passing each requirement through ionization are shown
 1056 in Table 2 for the full 2015 dataset and a simulated 1600 GeV, 10 ns lifetime
 1057 R-Hadron sample. The table highlights the overall acceptance \times efficiency for
 1058 signal events, which for this example is 19%. The major losses of signal events
 1059 occur first because of acceptance as only about 65% of events produce a charged
 1060 R-Hadron and in the metastable case only some of those particles propagate
 1061 through the pixel detector depending on the lifetime. The losses in efficiency
 1062 come primarily from requiring a well-measured, high-momentum track. Between
 1063 SM rejection and ionization, this signal region reduces the background of tracks
 1064 which pass the kinematic requirements down by an additional factor of almost
 1065 2000.

Selection	Exp. Signal Events	Observed Events in 3.2 fb^{-1}
Generated	26.0 ± 0.3	
E_T^{miss} Trigger	24.8 ± 0.3 (95%)	
$E_T^{\text{miss}} > 130 \text{ GeV}$	23.9 ± 0.3 (92%)	
Track Quality and $p_T > 50$	10.7 ± 0.2 (41%)	368324
Isolation Requirement	9.0 ± 0.2 (35%)	108079
Track $p > 150 \text{ GeV}$	6.6 ± 0.2 (25%)	47463
$m_T > 130 \text{ GeV}$	5.8 ± 0.2 (22%)	18746
Electron and Hadron Veto	5.5 ± 0.2 (21%)	3612
Muon Veto	5.5 ± 0.2 (21%)	1668
Ionization Requirement	5.0 ± 0.1 (19%)	11

Table 2: The expected number of events at each level of the selection for metastable 1600 GeV , 10 ns R-Hadrons, along with the number of events observed in data, for 3.2 fb^{-1} . The simulated yields are shown with statistical uncertainties only. The total efficiency \times acceptance is also shown for the signal.

12

1066

1067 BACKGROUND ESTIMATION

1068 12.1 BACKGROUND SOURCES

1069 12.2 PREDICTION METHOD

1070 12.3 VALIDATION AND UNCERTAINTY

13

1071

1072 SYSTEMATIC UNCERTAINTIES AND RESULTS

1073 13.1 SYSTEMATIC UNCERTAINTIES

1074 13.2 FINAL YIELDS

14

1075

1076 INTERPRETATION

1077 14.1 CROSS SECTIONAL LIMITS

1078 14.2 MASS LIMITS

1079 14.3 CONTEXT FOR LONG-LIVED SEARCHES

1080

PART VI

1081

CONCLUSIONS

1082

You can put some informational part preamble text here.

15

1083

1084 SUMMARY AND OUTLOOK

1085 15.1 SUMMARY

1086 15.2 OUTLOOK

1087

PART VII

1088

APPENDIX

1089

A

1090

1091 INELASTIC CROSS SECTION

B

1092

1093 APPENDIX TEST

1094 Examples: *Italics*, SMALL CAPS, ALL CAPS ¹. Acronym testing: **UML!** (**UML!**) –
1095 **UML! – UML! (UML!) – UML!s**

This appendix is temporary and is here to be used to check the style of the document.

1096 B.1 APPENDIX SECTION TEST

1097 Random text that should take up a few lines. The purpose is to see how sections
1098 and subsections flow with some actual context. Without some body copy be-
1099 tween each heading it can be difficult to tell if the weight of the fonts, styles,
1100 and sizes use work well together.

1101 B.1.1 APPENDIX SUBECTION TEST

1102 Random text that should take up a few lines. The purpose is to see how sections
1103 and subsections flow with some actual context. Without some body copy be-
1104 tween each heading it can be difficult to tell if the weight of the fonts, styles,
1105 and sizes use work well together.

1106 B.2 A TABLE AND LISTING

1107 Curabitur tellus magna, porttitor a, commodo a, commodo in, tortor. Donec in-
1108 terdum. Praesent scelerisque. Maecenas posuere sodales odio. Vivamus metus la-
1109 cus, varius quis, imperdiet quis, rhoncus a, turpis. Etiam ligula arcu, elementum a,
1110 venenatis quis, sollicitudin sed, metus. Donec nunc pede, tincidunt in, venenatis
1111 vitae, faucibus vel, nibh. Pellentesque wisi. Nullam malesuada. Morbi ut tellus ut
1112 pede tincidunt porta. Lorem ipsum dolor sit amet, consectetur adipiscing elit.
1113 Etiam congue neque id dolor.

1114 There is also a Python listing below Listing 1.

1 Footnote example.

LABITUR BONORUM PRI NO	QUE VISTA	HUMAN
fastidii ea ius	germano	demonstratea
suscipit instructior	titulo	personas
quaestio philosophia	facto	demonstrated

Table 3: Autem usu id.

115 B.3 SOME FORMULAS

Due to the statistical nature of ionisation energy loss, large fluctuations can occur in the amount of energy deposited by a particle traversing an absorber element². Continuous processes such as multiple scattering and energy loss play a relevant role in the longitudinal and lateral development of electromagnetic and hadronic showers, and in the case of sampling calorimeters the measured resolution can be significantly affected by such fluctuations in their active layers. The description of ionisation fluctuations is characterised by the significance parameter κ , which is proportional to the ratio of mean energy loss to the maximum allowed energy transfer in a single collision with an atomic electron:

You might get unexpected results using math in chapter or section heads.
Consider the `pdfspacing` option.

$$\kappa = \frac{\xi}{E_{\max}} \quad (3)$$

E_{\max} is the maximum transferable energy in a single collision with an atomic electron.

$$E_{\max} = \frac{2m_e\beta^2\gamma^2}{1 + 2\gamma m_e/m_x + (m_e/m_x)^2},$$

116 where $\gamma = E/m_x$, E is energy and m_x the mass of the incident particle, $\beta^2 =$
117 $1 - 1/\gamma^2$ and m_e is the electron mass. ξ comes from the Rutherford scattering
118 cross section and is defined as:

$$\xi = \frac{2\pi z^2 e^4 N_{Av} Z \rho \delta x}{m_e \beta^2 c^2 A} = 153.4 \frac{z^2}{\beta^2} \frac{Z}{A} \rho \delta x \text{ keV},$$

119 where

120 z charge of the incident particle
 N_{Av} Avogadro's number
121 Z atomic number of the material
122 A atomic weight of the material
123 ρ density
124 δx thickness of the material
125 κ measures the contribution of the collisions with energy transfer close to
126 E_{\max} . For a given absorber, κ tends towards large values if δx is large and/or if
127 β is small. Likewise, κ tends towards zero if δx is small and/or if β approaches
128 1.

2 Examples taken from Walter Schmidt's great gallery:
<http://home.vrweb.de/~was/mathfonts.html>

Listing 1: A floating example (`listings` manual)

```
1 for i in xrange(10):
    print i, i*i, i*i*i
print "done"
```

1125 The value of κ distinguishes two regimes which occur in the description of
1126 ionisation fluctuations:

- 1127 1. A large number of collisions involving the loss of all or most of the incident
1128 particle energy during the traversal of an absorber.

1129 As the total energy transfer is composed of a multitude of small energy
1130 losses, we can apply the central limit theorem and describe the fluctua-
1131 tions by a Gaussian distribution. This case is applicable to non-relativistic
1132 particles and is described by the inequality $\kappa > 10$ (i. e., when the mean
1133 energy loss in the absorber is greater than the maximum energy transfer
1134 in a single collision).

- 1135 2. Particles traversing thin counters and incident electrons under any condi-
1136 tions.

1137 The relevant inequalities and distributions are $0.01 < \kappa < 10$, Vavilov
1138 distribution, and $\kappa < 0.01$, Landau distribution.

- 1140 [1] ATLAS Collaboration. “The ATLAS Simulation Infrastructure”. In: *Eur.*
1141 *Phys. J. C* 70 (2010), p. 823. doi: [10.1140/epjc/s10052-010-1429-9](https://doi.org/10.1140/epjc/s10052-010-1429-9).
1142 arXiv: [1005.4568 \[hep-ex\]](https://arxiv.org/abs/1005.4568). SOFT-2010-01.
- 1143 [2] ATLAS Collaboration. “A study of the material in the ATLAS inner de-
1144 tector using secondary hadronic interactions”. In: *JINST* 7 (2012), P01013.
1145 doi: [10.1088/1748-0221/7/01/P01013](https://doi.org/10.1088/1748-0221/7/01/P01013). arXiv: [1110.6191 \[hep-ex\]](https://arxiv.org/abs/1110.6191).
1146 PERF-2011-08.
- 1147 [3] ATLAS Collaboration. *Summary of ATLAS Pythia 8 tunes*. ATL-PHYS-PUB-
1148 2012-003. 2012. url: <http://cds.cern.ch/record/1474107>.
- 1149 [4] ATLAS Collaboration. “Jet energy measurement with the ATLAS detector
1150 in proton–proton collisions at $\sqrt{s} = 7$ TeV”. In: *Eur. Phys. J. C* 73 (2013),
1151 p. 2304. doi: [10.1140/epjc/s10052-013-2304-2](https://doi.org/10.1140/epjc/s10052-013-2304-2). arXiv: [1112.6426 \[hep-ex\]](https://arxiv.org/abs/1112.6426). PERF-2011-03.
- 1153 [5] ATLAS Collaboration. “Single hadron response measurement and calorime-
1154 ter jet energy scale uncertainty with the ATLAS detector at the LHC”. In:
1155 *Eur. Phys. J. C* 73 (2013), p. 2305. doi: [10.1140/epjc/s10052-013-2305-1](https://doi.org/10.1140/epjc/s10052-013-2305-1). arXiv: [1203.1302 \[hep-ex\]](https://arxiv.org/abs/1203.1302). PERF-2011-05.
- 1157 [6] ATLAS Collaboration. “Electron and photon energy calibration with the
1158 ATLAS detector using LHC Run 1 data”. In: *Eur. Phys. J. C* 74 (2014), p. 3071.
1159 doi: [10.1140/epjc/s10052-014-3071-4](https://doi.org/10.1140/epjc/s10052-014-3071-4). arXiv: [1407.5063 \[hep-ex\]](https://arxiv.org/abs/1407.5063). PERF-2013-05.
- 1161 [7] ATLAS Collaboration. “Jet energy measurement and its systematic uncer-
1162 tainty in proton–proton collisions at $\sqrt{s} = 7$ TeV with the ATLAS detec-
1163 tor”. In: *Eur. Phys. J. C* 75 (2015), p. 17. doi: [10.1140/epjc/s10052-014-3190-y](https://doi.org/10.1140/epjc/s10052-014-3190-y). arXiv: [1406.0076 \[hep-ex\]](https://arxiv.org/abs/1406.0076). PERF-2012-01.
- 1165 [8] ATLAS Collaboration. “A measurement of the calorimeter response to sin-
1166 ggle hadrons and determination of the jet energy scale uncertainty using
1167 LHC Run-1 pp -collision data with the ATLAS detector”. In: (2016). arXiv:
1168 [1607.08842 \[hep-ex\]](https://arxiv.org/abs/1607.08842). PERF-2015-05.
- 1169 [9] ATLAS Collaboration. “Topological cell clustering in the ATLAS calorime-
1170 ters and its performance in LHC Run 1”. In: (2016). arXiv: [1603.02934](https://arxiv.org/abs/1603.02934)
1171 [hep-ex].
- 1172 [10] E. Abat et al. “Study of energy response and resolution of the ATLAS barrel
1173 calorimeter to hadrons of energies from 20 to 350 GeV”. In: *Nucl. Instrum.*
1174 *Meth. A* 621.1-3 (2010), pp. 134 – 150. doi: <http://dx.doi.org/10.1016/j.nima.2010.04.054>.

- 1176 [11] P. Adragna et al. "Measurement of Pion and Proton Response and Lon-
 1177 gitudinal Shower Profiles up to 20 Nuclear Interaction Lengths with the
 1178 ATLAS Tile Calorimeter". In: *Nucl. Instrum. Meth. A* 615 (2010), pp. 158–
 1179 181. doi: [10.1016/j.nima.2010.01.037](https://doi.org/10.1016/j.nima.2010.01.037).
- 1180 [12] S. Agostinelli et al. "GEANT4: A simulation toolkit". In: *Nucl. Instrum. Meth.*
 1181 A 506 (2003), pp. 250–303. doi: [10.1016/S0168-9002\(03\)01368-8](https://doi.org/10.1016/S0168-9002(03)01368-8).
- 1182 [13] N. S. Amelin et al. "Transverse flow and collectivity in ultrarelativistic
 1183 heavy-ion collisions". In: *Phys. Rev. Lett.* 67 (1991), p. 1523. doi: [10.1103/PhysRevLett.67.1523](https://doi.org/10.1103/PhysRevLett.67.1523).
- 1185 [14] N. S. Amelin et al. "Collectivity in ultrarelativistic heavy ion collisions". In:
 1186 *Nucl. Phys. A* 544 (1992), p. 463. doi: [10.1016/0375-9474\(92\)90598-E](https://doi.org/10.1016/0375-9474(92)90598-E).
- 1188 [15] B. Andersson, A. Tai, and B.-H. Sa. "Final state interactions in the (nuclear)
 1189 FRITIOF string interaction scenario". In: *Z. Phys. C* 70 (1996), pp. 499–
 1190 506. doi: [10.1007/s002880050127](https://doi.org/10.1007/s002880050127).
- 1191 [16] B. Andersson et al. "A model for low-pT hadronic reactions with general-
 1192 izations to hadron-nucleus and nucleus-nucleus collisions". In: *Nucl. Phys.*
 1193 B 281 (1987), p. 289. doi: [10.1016/0550-3213\(87\)90257-4](https://doi.org/10.1016/0550-3213(87)90257-4).
- 1194 [17] H. W. Bertini and P. Guthrie. "News item results from medium-energy
 1195 intranuclear-cascade calculation". In: *Nucl. Instr. and Meth. A* 169 (1971),
 1196 p. 670. doi: [10.1016/0375-9474\(71\)90710-X](https://doi.org/10.1016/0375-9474(71)90710-X).
- 1197 [18] L. V. Bravin et al. "Scaling violation of transverse flow in heavy ion col-
 1198 lisions at AGS energies". In: *Phys. Lett. B* 344 (1995), p. 49. doi: [10.1016/0370-2693\(94\)01560-Y](https://doi.org/10.1016/0370-2693(94)01560-Y).
- 1200 [19] L. V. Bravina et al. "Fluid dynamics and Quark Gluon string model - What
 1201 we can expect for Au+Au collisions at 11.6 AGeV/c". In: *Nucl. Phys. A* 566
 1202 (1994), p. 461. doi: [10.1016/0375-9474\(94\)90669-6](https://doi.org/10.1016/0375-9474(94)90669-6).
- 1203 [20] CMS Collaboration. "The CMS barrel calorimeter response to particle
 1204 beams from 2 to 350 GeV/c". In: *Eur. Phys. J. C* 60.3 (2009). doi: [10.1140/epjc/s10052-009-0959-5](https://doi.org/10.1140/epjc/s10052-009-0959-5).
- 1206 [21] H. S. Fesefeldt. *GHEISHA program*. Pitha-85-02, Aachen. 1985.
- 1207 [22] G. Folger and J.P. Wellisch. "String parton models in Geant4". In: (2003).
 1208 arXiv: [nucl-th/0306007](https://arxiv.org/abs/nucl-th/0306007).
- 1209 [23] B. Ganhuyag and V. Uzhinsky. "Modified FRITIOF code: Negative charged
 1210 particle production in high energy nucleus nucleus interactions". In: *Czech.
 1211 J. Phys.* 47 (1997), pp. 913–918. doi: [10.1023/A:1021296114786](https://doi.org/10.1023/A:1021296114786).
- 1212 [24] M. P. Guthrie, R. G. Alsmiller, and H. W. Bertini. "Calculation of the cap-
 1213 ture of negative pions in light elements and comparison with experiments
 1214 pertaining to cancer radiotherapy". In: *Nucl. Instrum. Meth.* 66 (1968), pp. 29–
 1215 36. doi: [10.1016/0029-554X\(68\)90054-2](https://doi.org/10.1016/0029-554X(68)90054-2).
- 1216 [25] J. Beringer et al. (Particle Data Group). "Review of Particle Physics". In:
 1217 *Chin. Phys. C* 38 (2014), p. 090001. URL: <http://pdg.lbl.gov>.

- 1218 [26] V.A. Karmanov. "Light Front Wave Function of Relativistic Composite
1219 System in Explicitly Solvable Model". In: *Nucl. Phys. B* 166 (1980), p. 378.
1220 doi: [10.1016/0550-3213\(80\)90204-7](https://doi.org/10.1016/0550-3213(80)90204-7).
- 1221 [27] Hung-Liang Lai, Marco Guzzi, Joey Huston, Zhao Li, Pavel M. Nadolsky,
1222 et al. "New parton distributions for collider physics". In: *Phys. Rev. D* 82
1223 (2010), p. 074024. doi: [10.1103/PhysRevD.82.074024](https://doi.org/10.1103/PhysRevD.82.074024). arXiv: [1007.2241 \[hep-ph\]](https://arxiv.org/abs/1007.2241).
- 1225 [28] A.D. Martin, W.J. Stirling, R.S. Thorne, and G. Watt. "Parton distributions
1226 for the LHC". In: *Eur. Phys. J. C* 63 (2009). Figures from the [MSTW Website](#),
1227 pp. 189–285. doi: [10.1140/epjc/s10052-009-1072-5](https://doi.org/10.1140/epjc/s10052-009-1072-5). arXiv: [0901.0002](https://arxiv.org/abs/0901.0002).
- 1229 [29] B. Nilsson-Almqvist and E. Stenlund. "Interactions Between Hadrons and
1230 Nuclei: The Lund Monte Carlo, Fritiof Version 1.6". In: *Comput. Phys. Com-*
1231 *mun.* 43 (1987), p. 387. doi: [10.1016/0010-4655\(87\)90056-7](https://doi.org/10.1016/0010-4655(87)90056-7).
- 1232 [30] K. A. Olive et al. "Review of Particle Physics". In: *Chin. Phys. C* 38 (2014),
1233 p. 090001. doi: [10.1088/1674-1137/38/9/090001](https://doi.org/10.1088/1674-1137/38/9/090001).
- 1234 [31] A. Ribon et al. *Status of Geant4 hadronic physics for the simulation of LHC*
1235 *experiments at the start of LHC physics program*. CERN-LCGAPP-2010-02.
1236 2010. URL: <http://lcgapp.cern.ch/project/docs/noteStatusHadronic2010.pdf>.
- 1238 [32] A. Sherstnev and R.S. Thorne. "Parton Distributions for LO Generators".
1239 In: *Eur. Phys. J. C* 55 (2008), pp. 553–575. doi: [10.1140/epjc/s10052-008-0610-x](https://doi.org/10.1140/epjc/s10052-008-0610-x). arXiv: [0711.2473](https://arxiv.org/abs/0711.2473).
- 1241 [33] T. Sjöstrand, S. Mrenna, and P. Skands. "A Brief Introduction to PYTHIA
1242 8.1". In: *Comput. Phys. Commun.* 178 (2008), pp. 852–867. doi: [10.1016/j.cpc.2008.01.036](https://doi.org/10.1016/j.cpc.2008.01.036). arXiv: [0710.3820](https://arxiv.org/abs/0710.3820).
- 1244 [34] Peter Speckmayer. "Energy Measurement of Hadrons with the CERN AT-
1245 LAS Calorimeter". Presented on 18 Jun 2008. PhD thesis. Vienna: Vienna,
1246 Tech. U., 2008. URL: <http://cds.cern.ch/record/1112036>.

1247 DECLARATION

1248 Put your declaration here.

1249 *Berkeley, CA, September 2016*

1250

Bradley Axen

1251

1252 COLOPHON

1253

Not sure that this is necessary.